New constraints on the late Quaternary landscape evolution of the eastern Tibetan Plateau from [10]Be and [26]Al in-situ cosmogenic nuclides

Ye Yang [a, b, c], Cong-Qiang Liu [a, b, **], Jérôme Van der Woerd [d, *], Sheng Xu [a, ***], Li-Feng Cui [b], Zhi-Qi Zhao [e, b], Qi-Lian Wang [b], Guo-Dong Jia [a], François Chabaux [c, ****]

[a] Institute of Surface-Earth System Science, Tianjin University, Tianjin 300072, China
[b] State Key Laboratory of Environmental Geochemistry, Institute of Geochemistry, Chinese Academy of Sciences, Guiyang 550081, China
[c] Laboratoire d'Hydrologie et de Géochimie de Strasbourg (LHyGeS), CNRS UMR 7517, University of Strasbourg, 1 rue Blessig, 67084 Strasbourg cedex, France
[d] Institut de Physique du Globe de Strasbourg (IPGS), CNRS UMR 7516, University of Strasbourg, 5 rue René Descartes, 67084 Strasbourg cedex, France
[e] School of Earth Sciences and Recourses, Chang'an University, Xi'an 710054, China

ARTICLE INFO

ABSTRACT

Based on Terrestrial Cosmogenic Nuclide (TCN) constraints from depth profiles of one granitic regolith from Wumingshan and five fluvial terraces from Xianshuihe and Zagunao rivers, we discuss the timing of the last deglaciation, the landscape-scale denudation and fluvial incision rates across the eastern Tibetan Plateau, in relation to previous work. We present a three-dimensional-graph visualization approach and corresponding constraints to better assess the feasibility and applicability of cosmogenic nuclides depth-profile dating. The exposure age (older than 19.4 ka) of the Wumingshan regolith corresponds to the retreat of the palaeo-Daocheng ice cap, which covered the Yidun terrane during the Last Glacial Maximum (LGM). Most basin-wide denudation rate data in the eastern Tibetan Plateau are lower than 130 mm/ka (47%, n = 90), which is consistent with the Wumingshan regolith denudation rate (lower than 52.8 mm/ka), and thus indicate that the landscape-scale denudation has been stabilized after the last deglaciation. Considering the reduction of integrated bulk density due to the accumulation of lower-density loess, we estimate mean exposure ages of Xianshuihe and Zagunao river terraces of 4.0 ± 0.7 ka, 5.9 ± 0.3 ka, 13.4 ± 2.0 ka, and 16.6 ± 1.4 ka. The observed increase in incision rate from 0.39 mm/yr over long timescale (~600 ka) to 5.88 mm/yr over the last 15 ka at the Xianshuihe river site is probably due to the transition from glacial to interglacial climatic conditions. The fewer abandoned terraces along the Zagunao river after the Heinrich event 1 (H1) indicates that the climate change during the latest glacial-interglacial transition impacted less the landscape evolution in a relatively lower elevation area. Comparison with previously reported fluvial incision rates elsewhere across the eastern margin of the Tibetan Plateau indicates that incision rates are mainly influenced by abrupt climate change or intensified summer monsoon since the early Holocene, but probably controlled by regional tectonic uplift or fluvial headward retreat as the timescale increases. Overall, we propose a synthetic pattern of landscape evolution mainly dominated by long-term tectonic uplift together with fluvial headward erosion, episodically influenced by climatic change throughout the late Quaternary.

© 2019 Elsevier Ltd. All rights reserved.

* Corresponding author.
** Corresponding author. Institute of Surface-Earth System Science, Tianjin University, Tianjin 300072, China.
*** Corresponding author.
**** Corresponding author.
E-mail addresses: liucongqiang@vip.skleg.cn (C.-Q. Liu), jerome.vanderwoerd@unistra.fr (J. Van der Woerd), sheng.xu@tju.edu.cn (S. Xu), fchabaux@unistra.fr (F. Chabaux).

1. Introduction

Topography is a result of the interaction of tectonic uplift and fluvial incision modulated by climate on geological time scales (Molnar et al., 1994, 2010; Kirby et al., 2000; Hancock and Anderson, 2002; Clark et al., 2005; Liu-Zeng et al., 2008; Pan et al., 2009; Ouimet et al., 2010; Perrineau et al., 2011; Finnegan et al., 2014). The recent evolution of the gentle gradient of the

topography of the southeastern Tibetan Plateau has been explained by two controversial models. On one hand, topography is considered as the result of external processes involving a wave of regressive development of rivers from the margin towards the interior of an-already-high continental plateau, initiated by the onset of the monsoon in the Miocene and modulated by climate (e.g., Métivier et al., 1998; Tapponnier et al., 2001; Liu-Zeng et al., 2008; Roger et al., 2010). On the other hand, it is interpreted as resulting from the recent eastward spread of ductile lower crust from the plateau center towards its rim (e.g., Burchfiel et al., 1995; Royden et al., 1997; Clark and Royden, 2000; Clark et al., 2005; Wang et al., 2012). Several approaches have been used to independently constrain the rates of tectonic uplift, erosion and the role of climate. Regional exhumation rates determined from thermochronology or cosmogenic isotopes are classically used to discuss the variations in space and time of regional uplift (Burbank et al., 1996; Kirby et al., 2002; Godard et al., 2010; Ouimet et al., 2010; Ansberque et al., 2015; Liu-Zeng et al., 2018; Tian et al., 2018). Fluvial terrace dating is commonly used to determine rates of river incision (Kirby et al., 2000; Liu et al., 2006, 2015; Chen et al., 2008b; Kong et al., 2009; Godard et al., 2010; Zhao et al., 2013; He et al., 2015; Zhang et al., 2018). The major issue with these approaches is how to disentangle regional tectonic uplift, climate change, and river dynamics from both exhumation and incision rates.

The objective of this study is to discuss our ability to determine tectonic exhumation rates from river incision rates derived from well dated inset terraces of two rivers in different tectonic setting (left-lateral strike-slip Xianshuihe Fault system and Longmenshan thrust belt) using in situ cosmogenic isotopes and by comparing these data with regionally published data. The analysis of one granite regolith provides a perspective to the coupling relationship between a surface erosive event caused by the glacial advance and retreat, and the possible source of fluvial sediments. This study also validates the methodology and emphasizes the need for short- (10s ka) and long-term (several 100s ka) chronologies to be able to constrain the long-term exhumation signal from the short-term climatic response of river systems.

2. Geological setting and sample descriptions

2.1. Study area

The eastern margin of the Tibetan Plateau is characterized by a low-relief, upland erosion surface (Burchfiel et al., 1995; Royden et al., 1997; Clark and Royden, 2000; Clark et al., 2004, 2005, 2006; Liu-Zeng et al., 2008) that is drained by the Jinsha, Lancang (Mekong), Nu (Salween), and Yellow rivers (Fig. 1a). The geological structure of the study area is characterized by two main tectonic units: 1) the Songpan Ganzi fold belt including Triassic flysch intruded by a series of Jurassic granitic plutons, deformed Paleozoic rocks, crystalline Precambrian basement, low grade metamorphic Mesozoic sedimentary rocks, and limited Cenozoic sediments (e.g., Yin and Harrison, 2000; Roger et al., 2008); 2) the Longmenshan range made of exhumed crystalline rocks of the Yangtze craton and Paleozoic passive margin sediments (e.g., Burchfiel et al., 1995). Climatically, the study region has significant spatial and temporal variations in precipitation, which are dominated by the east Asian monsoon, the Indian monsoon, and the Westerlies (Fig. 1) (e.g., Maussion et al., 2014). Mean annual precipitation decreases from the margin (~2000 mm/yr) towards the plateau (lower than ~500 mm/yr) (Bookhagen, 2018, see Fig. 1b).

2.1.1. Wumingshan regolith

The sampling site (~4000 m above sea level, Table 1) is located in southern Yidun terrane (or Shaluli mountain), surrounded by the

Qiangtang Terrane to west, the Songpan-Ganzi Fold Belt to northeast and the Yangtze Craton to southeast. It is bordered by the Jinshajiang Suture Zone (JSZ) in the west and Ganzi-Litang Suture Zone (GLSZ) in the east (Fig. 1a). Wumingshan regolith is a typical granitic weathering product for studying the local landscape evolution in this area. The sampling location avoids the cover of loess and the presence of colluvial deposition to ensure that the granitic regolith is derived from the underlying bedrock and formed as a vertical weathering profile. The targeted bedrock is a Late Triassic granitic pluton with a zircon U-Pb age of 225 ± 2 Ma (Wu et al., 2017). The slope gradient of the hill is about 25°. Mean annual precipitation and temperature are, respectively, 654.3 mm/yr and 4.8 °C for the period of 1981–2010 (data from National Meteorological Information Center, China; http://data.cma.cn/en). Previous works suggest that the palaeo-Daocheng Ice Cap with an extension of about 4000 km^2 covered the Yidun terrane during the Last Glacial Maximum (LGM) (Xu and Zhou, 2009; Fu et al., 2013; Zhang et al., 2015).

### 2.1.2. Xianshuihe and Zagunao fluvial terraces

The sampling sites of the fluvial terraces along the Xianshuihe river (~3150 m above sea level in our study area, Table 1), a tributary of the Yalong River (Fig. 1a), are located southeast of Luhuo County (Fig. 2b). The recent tectonic activity in this high continental plateau area is mainly controlled by the left-lateral strike-slip Xianshuihe Fault system (Fig. 1a) that triggered more than 20 earthquakes of magnitude higher than 6.5 since A.D. 1700, including the 2010 M_w 6.9 Yushu earthquake (Chevalier et al., 2017, and references therein). Mean annual precipitation and temperature are, respectively, 694.0 mm/yr and 6.7 °C for the period of 1981–2010 (data from National Meteorological Information Center, China; http://data.cma.cn/en). The arcuate Xianshuihe segmented fault system mainly consists of the Yushu-Ganzi Faults (YGF) to the northwest, the Xianshuihe Fault (XSHF) in the middle, and the Xiaojiang Fault (XJF) to the southeast (Fig. 1a) (e.g., Wang and Burchfiel, 2000).

The sampling sites along the Zagunao river (~1800 m above sea level in our study area, Table 1), a tributary of the Minjiang river (Fig. 1a), are located in Li County (Fig. 2c), a few kilometers upstream the main faults of the Longmenshan thrust belt (LMSTB) at the eastern margin of the Tibetan Plateau. The active LMSTB and Minjiang Fault (MJF), along which the devastating 2008 M_w 7.9 Wenchuan and 2013 M_w 7.0 Lushan earthquakes occurred, play a main role in the evolution of topographic and structural features at the eastern margin of the Tibetan Plateau. Mean annual precipitation and temperature are, respectively, 619.2 mm/yr and 11.4 °C for the period of 1981–2010 (data from National Meteorological Information Center, China; http://data.cma.cn/en).

In these two study areas, the abandoned fluvial sediments are covered with over than 50 cm-thick loess at all the sampling sites. The widely distributed loess is proposed to originate from the arid interior of the Tibetan Plateau during the late Quaternary (Qiao et al., 2014; Hu et al., 2015).

2.2. Sampling strategy

Thirty ~4 kg samples, including granitic regolith, amalgamated sands and sandy to pebbly gravels (Fig. 3), were collected (Fig. 1a). The artificial road cuts, modern river erosion profiles and natural gullies (Fig. 3) provided the ideal sampling sites. Samples were analyzed for in situ cosmogenic ^{10}Be and ^{26}Al in quartz. A digital elevation model (DEM) with 30 m resolution was constructed to determine the topographic environment (data from Geospatial Data Cloud site, Computer Network Information Center, Chinese Academy of Sciences; http://www.gscloud.cn). Conservative
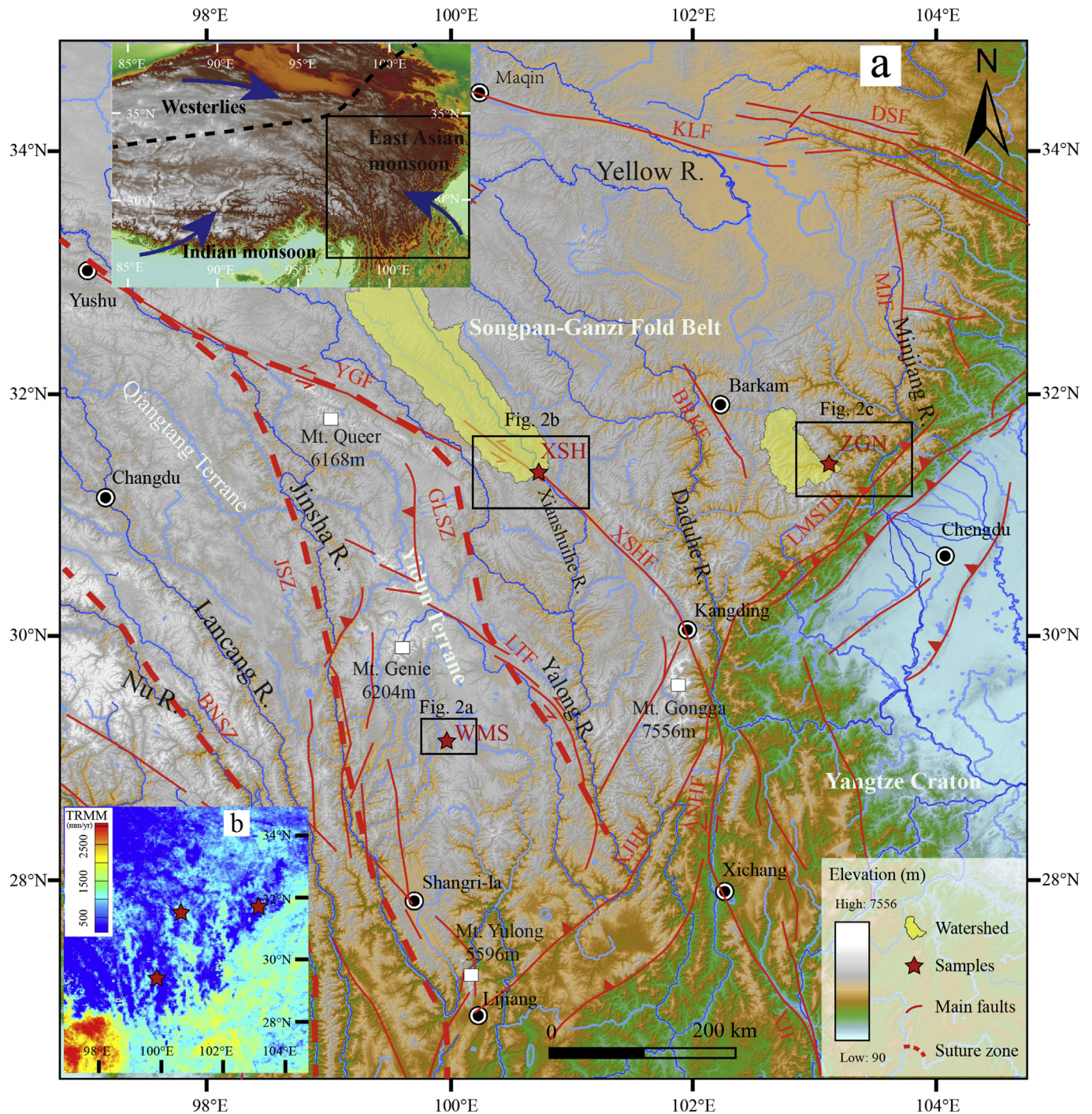
Fig. 1. (a) Topographic map of eastern Tibetan Plateau based on 90-m-resolution Shuttle Radar Topography Mission (SRTM) digital elevation model and major geologic structures (modified from Tapponnier et al., 2001; Clark et al., 2005; Taylor and Yin, 2009; Wu et al., 2017; Liu-Zeng et al., 2018). YGF, Yushu-Ganzi Fault; XSHF, Xianshuihe Fault; ANHF, Anninghe Fault; XJF, Xiaojiang Fault; LTF, Litang Fault; MJF, Minjiang Fault; KLF, Kunlun Fault; XJHF, Xiaojinhe Fault; BRKF, Barkam Fault; DSF, Dianshan Fault; BNSZ, Bangongcuo-Nujiang Suture Zone; JSZ, Jinshajiang Suture Zone; GLSZ, Ganzi-Litang Suture Zone; LMSTB, Longmenshan Thrust Belt. Inset: Location of study area. Dashed line represents transition between Eastern Asian monsoon, Indian monsoon and Westerlies (Gao, 1962). (b) Spatial distribution of annually averaged precipitation in eastern Tibetan Plateau from Tropical Rainfall Measuring Mission (TRMM) data (Bookhagen, 2018).

uncertainties of 10% on elevations were considered to account for field measurement error and morphological roughness.

The Wumingshan regolith profile was sampled to constrain the recent Quaternary weathering process and denudation rate of the granitic bedrock. To avoid the disturbing effect of shallow soil in the 2 m-deep profile, four deep samples were selected to determine the cosmogenic nuclides concentration in quartz (Fig. 3a and Table 2).

Considering the complex deposition history of loess, three depth-profiles and three deep burial samples were collected from the younger terraces in the Xianshuihe fluvial terraces (Fig. 3c–e). Coarse-grained quartz (>2 mm, XSH-5-1) and fine-grained quartz (<2 mm, XSH-5-2) were analyzed on duplicate samples to test the variability of inheritance in the different quartz source regions (Table 2). Two depth profiles and four deep burial samples (Table 2)

Table 1
Sampling sites, scaled surface cosmogenic ^{10}Be and ^{26}Al production rates and modeled exposure ages.

Sample	Latitude (N)	Longitude (E)	Elevation (m)	Height above river (m)	Shielding factor[a]	Loess thickness (cm)	P10$_{spal}$[b] (at g^{-1} a^{-1})	P10$_{slow}$[c] (at g^{-1} a^{-1})	P10$_{fast}$[c] (at g^{-1} a^{-1})	P26$_{spal}$[b] (at g^{-1} a^{-1})	P26$_{slow}$[c] (at g^{-1} a^{-1})	P26$_{fast}$[c] (at g^{-1} a^{-1})	Be age[d] (ka)	Be incision rate[e] (mm/yr)	Al age[d] (ka)	Al incision rate[e] (mm/yr)
Depth profile																
WMS1	29.1393	99.9623	3789	–	0.9458	0	39.63	0.0489	0.0777	261.3	3.4232	0.1613	>19.4	<52.8 mm/ka[f]	>27.8	<43.7 mm/ka[f]
XSH-2	31.3470	100.7273	3152	29 ± 3	0.9945	80	30.92	0.0417	0.0734	204.0	2.9193	0.1524	5.9 ± 1.3	4.9 ± 1.1	5.6 ± 2.0	5.2 ± 1.9
XSH-3	31.3468	100.7272	3144	21 ± 2	0.9945	40	30.85	0.0416	0.0733	203.5	2.9153	0.1523	4.0 ± 0.7	5.3 ± 0.9	1.2 ± 1.0	17.5 ± 14.6
XSH-5	31.3495	100.7241	3205	82 ± 8	0.9968	55	32.04	0.0426	0.0743	211.3	2.9827	0.1543	13.4 ± 2.0	6.1 ± 1.0	19.0 ± 2.3	4.3 ± 0.6
ZGN-2	31.4461	103.1700	1980	149 ± 15	0.9873	140	14.83	0.0272	0.0589	97.9	1.9060	0.1222	–	–	–	–
ZGN-7	31.4577	103.1708	1821	9 ± 1	0.9829	125	13.27	0.0255	0.0568	87.6	1.7853	0.1180	16.6 ± 1.4	0.5 ± 0.1	18.0 ± 3.7	0.5 ± 0.1
Burial samples																
XSH-4	31.3453	100.7288	3147	24 ± 3	0.9945	–	30.91	0.0417	0.0734	203.82	2.9183	0.1524	–	–	–	–
XSH-6	31.3556	100.7244	3155	7 ± 1	0.9936	–	31.03	0.0418	0.0734	204.64	2.9235	0.1525	–	–	–	–
ZGN-3	31.4451	103.1716	1916	85 ± 9	0.9834	–	14.15	0.0265	0.0579	93.38	1.8527	0.1202	–	–	–	–
ZGN-4	31.4487	103.1731	1894	68 ± 7	0.9834	–	13.94	0.0262	0.0576	92.02	1.8371	0.1197	–	–	–	–
ZGN-5	31.4516	103.1725	1859	35 ± 4	0.9805	–	13.58	0.0258	0.0571	89.61	1.8072	0.1186	–	–	–	–
ZGN-6	31.4524	103.1730	1833	13 ± 2	0.9834	–	13.38	0.0256	0.0570	88.30	1.7945	0.1183	–	–	–	–

^{10}Be spallogenic production rates (SLHL) is 4.13 atoms/(g(qtz) yr) (Martin et al., 2017). The ^{26}Al/^{10}Be spallogenic production ratio induced by the standardization used at ASTER is 6.61 ± 0.52. Slow and fast muons production rates (SLHL: 0.012 atom/(g(qtz) yr) and 0.039 atom/(g(qtz) yr) for ^{10}Be and 0.84 atom/(g(qtz) yr) and 0.081 atom/(g(qtz) yr) for ^{26}Al, respectively) are only scaled relatively to atmospheric pressure (Braucher et al., 2011).
a Determined by CRONUS online calculator (Balco et al., 2008).
b As stated by Stone (2000).
c According to Braucher et al. (2011).
d Calculated from results of model 2 (mean age).
e Average incision rate from formation of fluvial terrace to present.
f Denudation rate of Wumingshan regolith in mm/ka.

were collected from the younger terraces in the Zagunao fluvial terraces. These abandoned sediments were collected to constrain the exposure age of the fluvial terraces and the incision rate of the river. The loess mantle, the fine fraction (silt and soil), and the coarse material (sand, pebbles, cobbles, and boulders) were assumed to have densities of 1.4 ± 0.1, 1.6 ± 0.1, and 2.6 ± 0.1 g/cm^3, respectively. The bulk density was calculated by estimating the proportion of fine and coarse fractions using field photos and macroscopic description of the horizons (Hancock et al., 1999; Perrineau et al., 2011; Guilbaud et al., 2017).

3. Analytical methods

3.1. TCN sample preparation and analyses

Chemical preparation was performed at the cosmogenic nuclide laboratory of Institut de Physique du Globe de Strasbourg (UMR 7516, CNRS and University of Strasbourg, France) following standard methods (e.g., Perrineau et al., 2011; Guilbaud et al., 2017). Samples were crushed and sieved to fractions of 250−500 μm followed by magnetic and gravimetric separations. Oxides and carbonate matter were removed by HNO$_3$ leaching. Multiple overnight leaches in hot 1% HF/HNO$_3$ solutions were performed to remove the meteoric cosmogenic nuclides and to obtain purified quartz. Samples were dissolved in 5:1 HF/HNO$_3$ and spiked with ~250 mg of commercially available Scharlau ICP 1000 mg/l ^{9}Be standard (Table 2). Scharlau ICP 1000 mg/l ^{27}Al standard was added for samples with less than 2 mg of native ^{27}Al determined with ICP-AES at LHyGeS (Table 2). Subsequently, the separation and purification by ion exchange chromatography, hydroxylation and oxidation were performed. BeO and Al$_2$O$_3$ were mixed with niobium and silver powder, respectively, to make targets. The ^{10}Be/^{9}Be and ^{26}Al/^{27}Al ratios were measured on the ASTER AMS French national facility (CEREGE, Aix-en-Provence, France) (Table 2). ^{10}Be/^{9}Be and ^{26}Al/^{27}Al ratios were calibrated versus the ASTER in-house standard STD-11 (^{10}Be/^{9}Be = (1.191 ± 0.013) × 10^{-11}) and SM-A1-11 (7.401 ± 0.064 × 10^{-12}), respectively (Arnold et al., 2010; Braucher et al., 2015). Both ^{10}Be/^{9}Be and ^{26}Al/^{27}Al ratios of processed blanks are approximately 3 × 10^{-15}.

3.2. Model setup

3.2.1. Chi-square modeling

Using the classical approximation that subsurface production rate can be represented by exponential functions different for neutrons, slow muons and fast muons (Granger and Smith, 2000; Schaller et al., 2002; Braucher et al., 2003, 2011, 2013; Hidy et al., 2010; Balco, 2017) and by making the presuppositions of steady erosion, average inheritance, and constant production rates, the expression of a measured nuclide concentration as a function of denudation rate, exposure age, and inheritance can be written in the following explicit form (Braucher et al., 2003, 2011; Siame et al., 2004; Rodés et al., 2011; Cui et al., 2014, 2016, 2014; Ackerer et al., 2016; Charreau et al., 2017; Schaller et al., 2018; Sordi et al., 2018):

$$C(x,\varepsilon,t) = c_0 e^{-\lambda t} + \sum_{i=spal,slow,fast} \frac{P_i}{\lambda + \frac{\rho_{loess}}{\Lambda_i}\varepsilon} e^{-\frac{\rho_x}{\Lambda_i}x}\left[1 - e^{-\left(\lambda + \frac{\rho_{loess}}{\Lambda_i}\varepsilon\right)t}\right]$$

(1)

where $C(x,\varepsilon,t)$ is the present nuclide concentration, c_0 is the average cosmogenic inheritance (in at/g), ρ_x is the integrated bulk density at depth x, t is the exposure age, ε is the accumulation rate (negative) or denudation rate (positive), λ is the decay constant
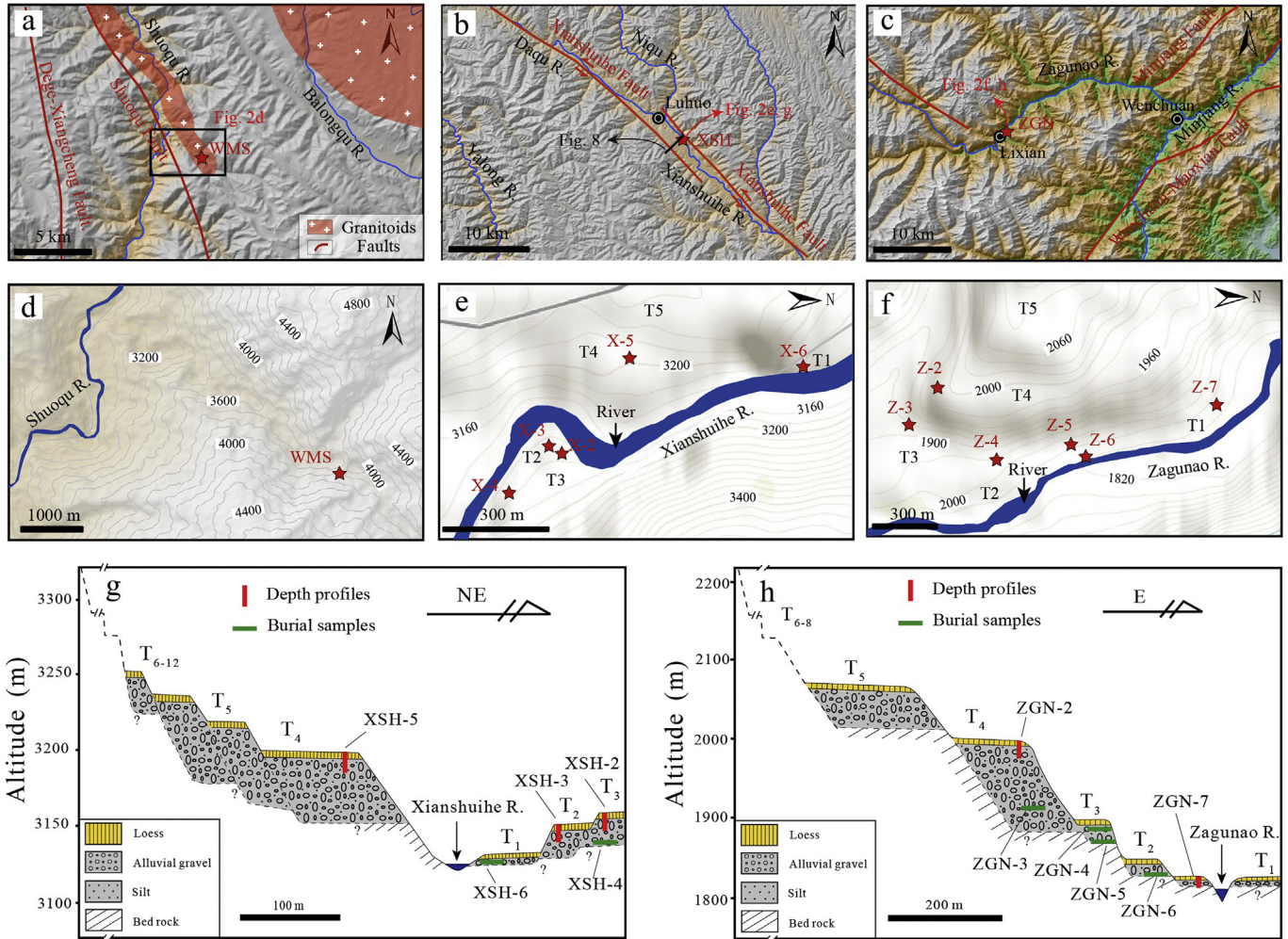
Fig. 2. Sample locations of Wumingshan regolith (a and d), Xianshuihe (b and e) and Zagunao rivers (c and f), superimposed on shaded relief and contour lines, respectively. (g) and (h) show cross-profile sketchs for Xianshuihe and Zagunao fluvial terrace sequences. Red bars indicate sampling sites of depth profiles. Green bars are burial samples. In b, black line is approximate position of synthetic section of Fig. 8. (For interpretation of the references to color in this figure legend, the reader is referred to the Web version of this article.)

5.00×10^{-7} yr^{-1} for ^{10}Be (Chmeleff et al., 2010; Korschinek et al., 2010) and 9.83×10^{-7} yr^{-1} for ^{26}Al (Nishiizumi, 2004), P_{spal}, P_{slow}, P_{fast} and Λ_{spal}, Λ_{slow}, Λ_{fast} are the surface production rates and attenuation lengths of neutrons, slow muons and fast muons, respectively. An exponential model for muon production rates provides an acceptable accuracy for shallow depth profiles and relatively slow denudation rates as found at our study sites. Therefore, the simplified three exponential functions approximation for subsurface production rates was used in all calculations and modeling in this study. The production rates relative to sea level and high latitude (SLHL) as a function of geographic latitude and air pressure (Lal, 1991; Stone, 2000) are listed in Table 1. A global mean SLHL spallogenic production rate of 4.13 at/(g$_{(qtz)}$ yr) for ^{10}Be (Martin et al., 2017) and a ^{26}Al/^{10}Be spallogenic production ratio of 6.61 (Braucher et al., 2011) are used to scale the local production rates. We also include a correction factor for shielding by the surrounding topography using the online calculator of Balco et al. (2008) and regard the shielding by snow or vegetation as negligible. The spallogenic production rates uncertainty of ^{10}Be and ^{26}Al are assumed to be 7.2% and 10% (Phillips et al., 2016), respectively, after Borchers et al. (2016) by integrating the root mean square error of different previous study sites. Muons production rates (see Table 1) are scaled with atmospheric pressure and we ignore the latitudinal effect (Braucher et al., 2011). Depth scaling of production rates are based on attenuation lengths Λ_{spal}, Λ_{slow}, and Λ_{fast} of ~165, ~1500, and ~4320 g/cm^2 respectively (Braucher et al., 2011; Marrero et al., 2016). The best fit was performed by minimizing the chi-square value (Rodés et al., 2011, and references therein) as follows:

$$\chi^2 = \sum_{i=1}^{n} \left(\frac{C_i - C(x, \varepsilon, t)}{\sigma_{C_i}} \right)^2 \qquad (2)$$

where C_i are the measured concentration at x_i depth, and $C(x, \varepsilon, t)$ is the concentration predicted from Equation (1). Only the uncertainty of the measured concentration (σ_{C_i}) is considered because it would be impossible to simultaneously fit all parameters using only one measured concentration per sample (Borchers et al., 2016). Recently, in order to avoid the problem of "mixed estimator", the $\chi^2_{1\sigma}$ was replaced by the value of $\chi^2_{min} + 1$ (Guralnik et al., 2011; Saint-Carlier et al., 2016; Charreau et al., 2017; Delmas et al., 2018) to obtain the fitting values since the range of solutions is considered as a proxy for 1σ confidence level (Bevington and Robinson, 2003). To estimate the goodness of the fitting, the p-value of the chi-square best fit value has been used in this study, and p-values larger than 5% are considered as a valid prediction of the fitting model (Aster et al., 2013; Borchers et al., 2016; Phillips et al., 2016).

Fig. 3. (a—b) Field photographs of Wumingshan regolith showing the vertical section with clear boundary between bedrock and overlying saprolite. (c—e) Field photographs showing location of sampling sites above Xianshuihe river and thick loess cover. (f—g) Field photographs showing five levels of fluvial terraces above Zagunao river and (h) important slope instabilities.

3.2.2. A three-dimensional-graph visualization approach

Based on previous approaches (Braucher et al., 2009; Hidy et al., 2010; Rodés et al., 2011; Marrero et al., 2016), a visual, multi-interpreted, and robust depth-profile simulation approach was designed to model the three parameters (denudation rate, exposure age, and inheritance) for cosmogenic nuclides depth profile (see detailed description in Appendix A). In practice, the chi-square value can be minimized by a series of different denudation rate, exposure age, and inheritance values even when the p-value is close to 1 (see detail in Fig. S.1). The inability to obtain a unique solution is inevitable for the square sum function. However, to circumvent this difficulty, the bounds of denudation rate, exposure age, or inheritance are constrained by various reliable assumptions, such as the effective total denudation evidence (Hidy et al., 2010; Marrero et al., 2016), a zero denudation (Guralnik et al., 2011; Saint-Carlier et al., 2016), or a considered inheritance (Cui et al., 2016; Hidy et al., 2018). All the assumptions constrain the final fit, so we should be cautious when choosing the various reliable assumptions. Overall, the resulting ranges are sufficiently reliable to avoid over-constraining the inversion while discouraging the complex modeling to calculate the unreliable ranges that are considered to be less likely. Therefore, the 3D-graph visualization approach is used in this study to estimate the impact of the different assumptions and display the interactions among denudation rate, exposure

Table 2
^{10}Be and ^{26}Al cosmogenic isotope data.

Sample	Depth[a] (cm)	Density[b] (g/cm³)	Qtz mass (g)	Total ^{9}Be (µg)	Total ^{27}Al (µg)	^{10}Be/^{9}Be[c] (10^{-14})	± (%)	[^{10}Be] (10^{4} at/g)	± (%)	^{26}Al/^{27}Al[d] (10^{-14})	± (%)	[^{26}Al] (10^{4} at/g)	± (%)
Wumingshan regolith													
WMS1-11	52.5	1.6	31.02	253	2300	155.06	2.9	76.06	3.5	325.78	2.8	559.97	3.4
WMS1-17	82.5	1.6	34.00	258	2534	144.83	2.8	66.13	3.5	300.74	2.7	519.40	3.4
WMS1-22	115	1.6	35.62	259	2554	122.89	2.9	53.79	3.5	240.74	3.1	400.04	3.7
WMS1-26	155	1.6	30.35	261	2221	87.23	3.4	45.13	4.0	189.52	3.8	321.46	4.3
Xianshuihe river													
XSH-2-1	60	2.2	11.86	228	1438	16.64	3.8	19.25	4.3	43.16	6.4	121.30	6.7
XSH-2-2	130	2.2	12.83	232	1514	11.16	3.9	12.11	4.4	27.76	6.6	75.88	6.9
XSH-2-3	180	2.2	12.42	238	1843	14.28	4.0	16.43	4.5	31.67	7.1	108.75	7.3
XSH-3-1	25	2.2	14.48	242	1566	17.97	3.8	18.06	4.3	41.32	6.0	103.55	6.3
XSH-3-2	70	2.1	4.61	257	1380	4.84	5.1	16.23	5.4	16.10	9.1	111.63	9.3
XSH-3-3	155	2.1	6.46	261	1382	5.00	4.6	12.14	5.0	18.24	8.2	90.43	8.5
XSH-5-1-1	15	2.2	11.80	262	2025	45.56	3.4	60.91	3.9	111.25	4.0	442.58	4.4
XSH-5-1-2	55	2.2	5.12	251	2441	15.90	4.0	46.94	4.4	57.72	3.1	638.21	3.7
XSH-5-1-3	115	2.2	14.44	253	3639	44.90	3.7	47.36	4.2	31.56	6.3	184.28	6.6
XSH-5-2-1	15	2.2	20.43	254	3468	85.43	3.4	63.80	4.0	125.68	3.1	494.49	3.7
XSH-5-2-2	55	2.2	23.02	252	3998	71.77	3.4	47.28	3.9	91.34	3.1	367.68	3.7
XSH-5-2-3	115	2.2	20.93	251	3800	58.58	3.6	42.20	4.1	71.43	4.2	300.57	4.6
XSH-4-1-	~2000	2.2	22.22	252	1528	11.61	3.8	7.92	4.3	42.01	6.2	66.96	6.5
XSH-4-2-	~2500	2.2	32.37	255	2838	18.24	3.7	8.66	4.2	31.58	4.0	64.15	4.5
XSH-6-	~500	2.2	36.60	254	4082	42.09	3.5	17.58	4.0	51.09	4.5	132.04	4.9
Zagunao river													
ZGN-2-1	24	2.2	14.56	261	5843	4.57	6.1	4.91	6.4	3.62	10.4	33.65	10.6
ZGN-2-2	147	2.2	11.55	254	2626	2.47	7.7	3.26	8.0	5.02	9.1	26.45	9.3
ZGN-2-3	270	2.2	15.14	265	38,400	4.90	6.0	5.15	6.4	0.56	34.1	33.10	34.2
ZGN-2-4	597	2.2	14.30	268	1922	3.35	5.5	3.77	5.9	8.79	12.5	27.37	12.6
ZGN-7-1	55	1.8	6.53	266	1873	4.06	5.5	9.95	5.9	12.70	9.5	84.38	9.7
ZGN-7-2	165	2.2	9.93	253	1973	2.91	6.6	4.45	6.9	9.39	11.0	43.24	11.2
ZGN-7-3	275	2.1	8.30	262	1769	1.59	9.2	3.01	9.4	6.36	26.6	31.42	26.7
ZGN-3	~2000	2.2	8.86	278	2291	2.50	6.4	4.72	6.7	4.51	10.3	27.01	10.5
ZGN-4	~2000	2.2	2.38	263	1655	0.80	13.5	5.29	13.7	2.34	23.2	37.60	23.2
ZGN-5	~1500	2.2	31.72	253	2156	2.52	6.4	1.21	6.7	7.16	12.8	11.28	13.0
ZGN-6	~1500	2.2	3.34	260	1684	0.52	20.7	2.43	20.8	1.80	24.4	21.01	24.5

Total ^{9}Be and ^{27}Al have been measured by inductively coupled plasma atomic emission spectrometry (ICP-AES) and uncertainty of 2% has been considered. ^{10}Be and ^{26}Al concentration measurements were performed at ASTER AMS (CEREGE, Aix-en-Provence, France). STD-11 and SM-A1-11 standard materials with isotope ratio ^{10}Be/^{9}Be of $(1.1911 \pm 0.013) \times 10^{-11}$ and ^{26}Al/^{27}Al of $(7.401 \pm 0.013) \times 10^{-12}$ have been used to measure ^{10}Be and ^{26}Al concentrations (Arnold et al., 2010; Braucher et al., 2015).
  [a] Total depth excluding loess thickness.
  [b] Average density of 1.6 g/cm³ has been assumed for regolith according to previous data (Ackerer et al., 2016; Cui et al., 2016); integrated bulk density excluding loess (1.4 g/cm³) for fluvial sediments.
  [c] Corrected by blank ratio (6.8 × 10⁻¹⁵ for Wumingshan regolith and average 2.9 × 10⁻¹⁵ of three blank ratios for Xianshuihe and Zagunao rivers).
  [d] Corrected by average blank ratio of 1.5 × 10⁻¹⁵.

age, and inheritance in one graph. This approach also emphasizes that any paired solutions of age and denudation rate are based on a given inheritance.

3.2.3. Variable-density approach

A significant loess cover is found covering the depth profiles, indicating that the assumption of a constant density based on the present-day outcrop, which includes the loess cover, is invalid. To account for the potential influence of loess after the abandonment of the fluvial terraces, we consider that the integrated bulk density composed of the lower-density covering loess and the higher-density underlying sediments increases or decreases constantly with time due to the denudation or accumulation of the loess in the study area. Equation (1) then becomes (see details in Appendix B):

$$C(x, \varepsilon, t) = c_0 e^{-\lambda t} + \sum_{i=spal,slow,fast} \frac{P_i}{\lambda + \frac{\rho_{loess}}{\Lambda_i}\varepsilon} e^{-\left(\frac{\rho_{xsed}x_{sed} + \rho_{loess}x_{loess}}{\Lambda_i}\right)} \left[1 - e^{-\left(\lambda + \frac{\rho_{loess}}{\Lambda_i}\varepsilon\right)t}\right]$$

(3)

where x_{loess} is the current depth of the loess, ρ_{xsed} is the integrated bulk density of sediments at depth x_{sed}, and ρ_{loess} is the density of the loess (Fig. B.1, see details in Appendix B).

To account for the potential effects of loess after abandonment of the fluvial terraces and without knowledge of the timing and rate of loess deposition, three different simplified deposition models

have been used to model the exposure ages (e.g., Charreau et al., 2017). Model 1: instantaneous loess deposition after terrace abandonment and post-deposition constant denudation (maximum age); Model 2: continuous loess deposition at a constant accumulation rate after terrace abandonment ("mean" age); Model 3: experience a constant terrace denudation before a very recent loess deposition event (minimum age; ignoring the attenuation in the loess) (Fig. B.1, see details in Appendix B).

4. Results

The concentrations of ^{26}Al and ^{10}Be show a linear relationship (Fig. 4a). The average ratio (~7.45) of $^{26}Al/^{10}Be$ is higher than the spallation production ratio of 6.61 (Braucher et al., 2011), which can be explained by the variation in $^{26}Al/^{10}Be$ ratio with increasing bedrock depth (Akçar et al., 2017). The $^{26}Al/^{10}Be$ ratios for all samples, excluding two anomalous results (XSH-5-1-2 and XSH-5-1-3), plot well in the steady state erosion island (Lal, 1991), which indicates that the pre-deposition burial history of the samples is negligible (Fig. 4b).

The results of the four cosmogenic nuclide ^{10}Be and ^{26}Al depth-profile saprolite samples (WMS1-11, WMS1-17, WMS1-22, and WMS1-26) are listed in Table 2 and supplementary Table 1. The ^{10}Be inversion of the depth profile, assuming the net erosion was no more than 100 cm ($\varepsilon \times t < 100$), constrains the age of the regolith to $27.0^{+9.6}_{-7.6}$ ka, the denudation rate to $18.4^{+14.4}_{-18.4}$ mm/ka, and the inheritance to $26.6^{+2.9}_{-3.1} \times 10^4$ at/g (Fig. 5a, Supplementary Table 1 and Fig. S.2). The constant inheritance is interpreted as a result of one erosive event caused by the impact of the last glacial period (see detail in section 5.2). Ignoring the constraint of net erosion, a minimum age of 19.4 ka and a maximum denudation rate of 52.8 mm/ka are obtained. The ^{26}Al inversion shows consistent results (see details in supplementary Table 1 and Fig. S.3). Similar ranges of age (21.6—38.6 ka), denudation rate (0—29.6 mm/ka) and ^{10}Be inheritance (23.3—28.4 × 10^4 at/g) (see details in supplementary Table 1) are calculated when combining ^{26}Al and ^{10}Be cosmogenic nuclides (Rodés et al., 2011, 2014) by assuming negligible pre-deposition burial history, or with the simulator of Hidy et al. (2010; version 1.2) (age: 19.3—36.5 ka; denudation rate: 0—33.1 mm/ka; inheritance: 22.9—29.5 × 10^4 at/g) (see details in Fig. S.4). Such a consistency between the three calculation approaches supports the reliability of the results derived from the depth

profiles and the assumption of negligible burial history.

The whole cosmogenic nuclide analyses of fluvial terraces are presented in Table 2 and supplementary Table 2. According to the depth profiles, we calculated the surface exposure age, accumulation/denudation rate, and inheritance of the fluvial sediments using the three-dimensional chi-square inversion approach. Three different models (see details in Appendix B) were used for each depth profile to estimate the impact caused by different loess deposition scenario. Based on the field observations, a loess net erosion of less than 20 cm was assumed in Model 1 to constrain the wide range of free parameters. There are no obvious paleosoil between the loess and the fluvial sediments, conservatively, no more than 10 cm net erosion was assumed in Model 3 to constrain the 3D-graph visualization inversion approach. The Model 2 inversion approach, assuming continuous deposition ($\varepsilon \times t = x_{loess}$) and considering the variation of the integrated bulk density, constrains the mean ^{10}Be exposure age to 4.0 ± 0.7 ka, 5.9 ± 1.3 ka, 13.4 ± 2.0 ka, and 16.6 ± 1.4 ka for the sites XSH-3 (T2), XSH-2 (T3), XSH-5 (T4), and ZGN-7 (T1), respectively (Fig. 4b–d, 4f and supplementary Table 2). The mean ^{26}Al exposure ages show consistent results (see details in Fig. S.3). Moreover, two end-member ages of the minimum exposure age (Model 1: instantaneous deposition of loess after terrace abandonment) and the maximum exposure age (Model 3: constant denudation before very recent loess deposition) are presented in Fig. 5 and supplementary Table 2.

Due to the scattering of the XSH-2 (T3) data and the small number of samples, the analytical quality of the XSH-2 (T3) age (5.9 ± 1.3 ka) is slightly less robust. However, this age is consistent with the position of T3 between T2 and T4 with ages of 4.0 ± 0.7 ka and 13.4 ± 2.0 ka, respectively (Fig. 5b). Owing to the tectonic activity and landslides in the Zagunao area (Fig. 2g and h), the data of the deepest (8 m) depth profile (ZGN-2) cannot be fitted due to excessive scatter and insufficient number of samples. We used forward modeling (e.g., Perrineau et al., 2011), assuming no denudation and a two-stages deposition model to constrain the two periods of exposure of ~2.0 ka and ~3.3 ka (Fig. 5e).

Coarse-grained quartz (2—10 mm, XSH-5-1) and fine-grained quartz (<2 mm, XSH-5-2) were analyzed on 3 samples to test whether the various quartz grains have different inheritance values. The ^{10}Be results show very similar concentrations for the two shallow samples but a larger concentration for the deepest
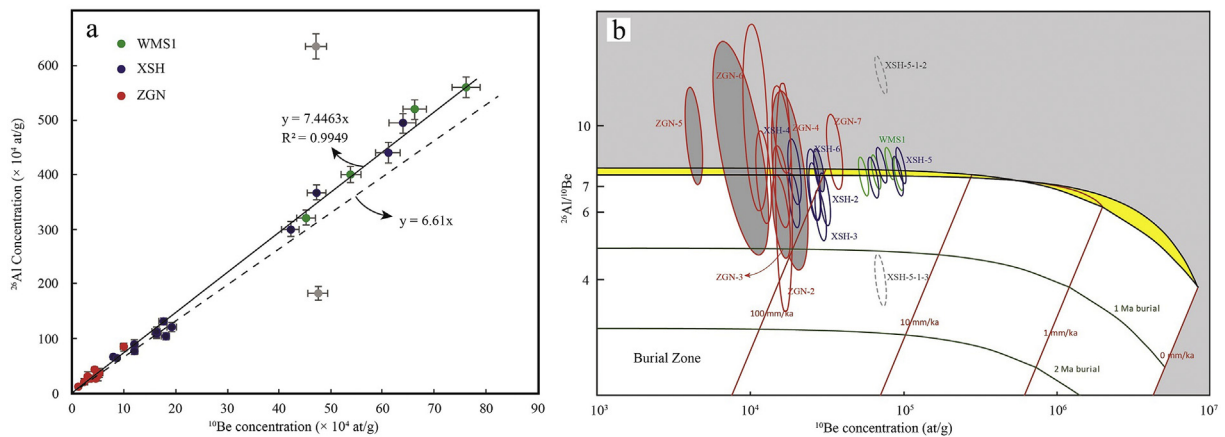
Fig. 4. (a) Correlation of ^{10}Be and ^{26}Al concentrations. Solid line is best fit, excluding two outliers (grey circles). Black dashed line presents production ratio of $^{26}Al/^{10}Be = 6.61$ following Braucher et al. (2011). (b) Normalized $^{26}Al/^{10}Be$ ratios plotted against ^{10}Be concentrations (modified from Vermeesch (2007) and scaled to SLHL). Steady-state erosion island (shaded yellow) showing saturation values for $^{26}Al/^{10}Be$ for different erosion rates (red line). Open ellipses represent depth profile samples with 2σ uncertainties. Shaded grey ellipses are burial samples, excluding two outliers (dashed ellipses). (For interpretation of the references to color in this figure legend, the reader is referred to the Web version of this article.)
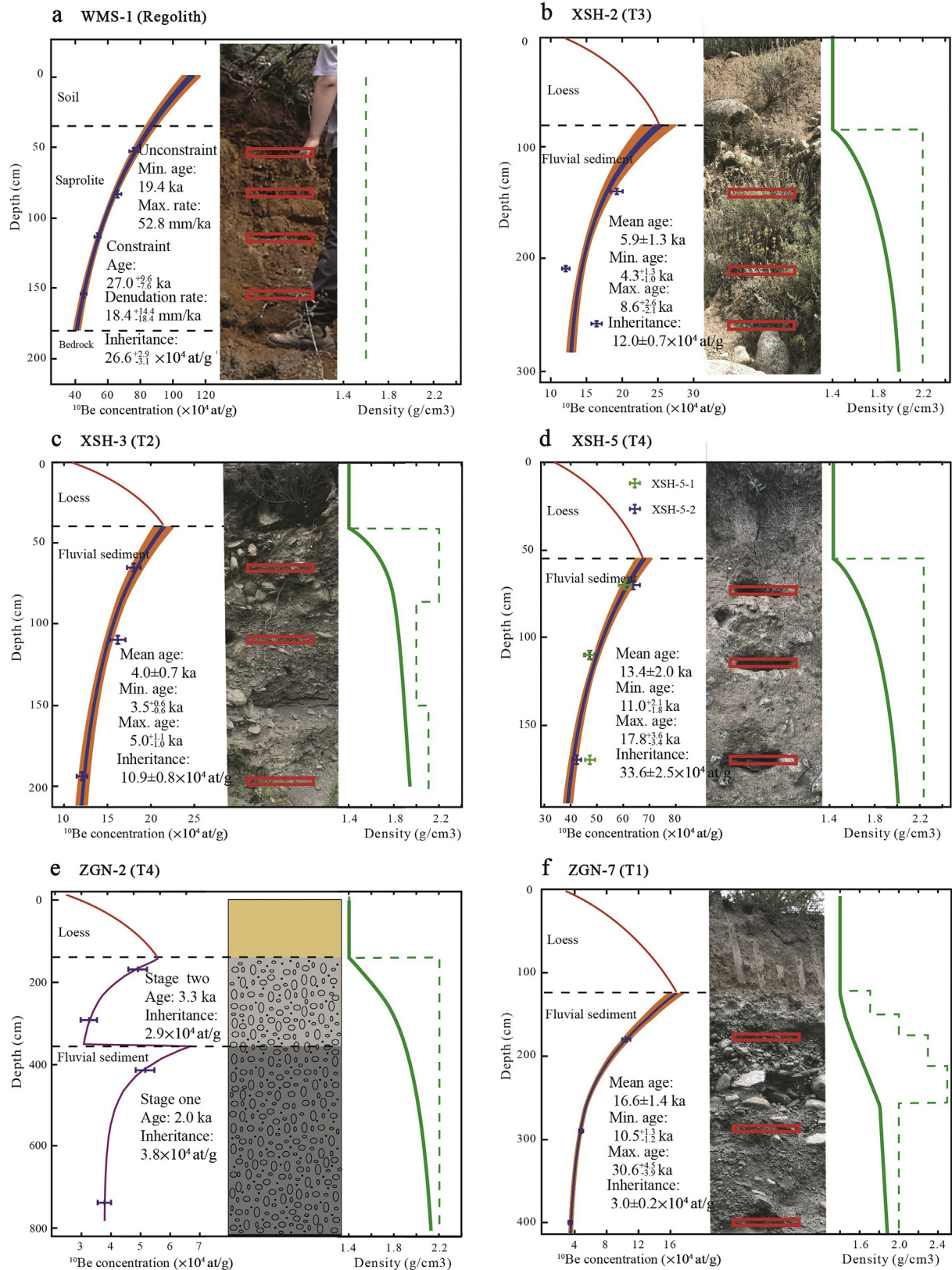
Fig. 5. Cosmogenic [10]Be depth profile data, field photographs and integrated bulk density of Wumingshan regolith (a), Xianshuihe (b, c, and d) and Zagunao rivers (e and f). Orange and blue curves show fitting solutions that match χ^2 values within limits of $[\chi^2_{min}; \chi^2_{min} +1]$ and best group with smallest χ^2 values ($\chi^2_{min} \times 1.01$), respectively. Red curves show variation of nuclide concentration in loess under the assumption of a constant inheritance. Inset text gives exposure age, denudation rate, and inheritance. Solid and dashed green lines, respectively, show integrated bulk density and bulk density. Purple curve shows forward model solution (e.g., Perrineau et al., 2011) with two-stages model. (For interpretation of the references to color in this figure legend, the reader is referred to the Web version of this article.)

coarse-grained quartz. The difference observed in the deepest sample may be explained by a difference in the provenance of the coarse-grained quartz and fine-grained quartz. The coarse-grained quartz could be detached from resistant quartz veins, which have a longer residence time on the hillslopes (e.g., Codilean et al., 2014), recycled from the older sediments, thus with a longer exposure than the fresh rocks (e.g., Wittmann et al., 2011), or derived from the abrasion of cobbles exhumed at high elevations (e.g., Carretier et al., 2015). The result highlights the importance of grain size in the interpretation of cosmogenic nuclide data.

5. Discussion

5.1. Feasibility and applicability of the three-dimensional-graph visualization approach for cosmogenic nuclides depth profile

The values derived from the three-dimensional-graph visualization approach provide a reliable estimate of exposure age, denudation rate, and inheritance. However, the chi-square value (Equation (3)) can be minimized for different sets of denudation rates, exposure ages, and inheritance values (e.g., Hidy et al., 2010; Borchers et al., 2016; Saint-Carlier et al., 2016). Even when a local minimum chi-square value is obtained, including the perfect fit of the data (p-value = 1), one can still get a series of possible solutions for exposure ages and denudation rates (Figs. S.1, S.2a and 2b). The self-check of the three-dimensional inversion approach indicates that the assumptions of negligible inheritance or subjective denudation rate should not be made to gain a seemingly plausible exposure age, e.g., exposure dating of surface samples (surface rock, surface sediments and moraine) and excessive constraints should not be imposed to the simulator. Therefore, independent constraints derived from the field investigations are essential to obtain a reliable solution (see details in section 4).

5.2. The timing of the last deglaciation revealed by receding glacier in the eastern Tibetan Plateau

The glacial history of the eastern Tibetan Plateau has been investigated to constrain the timing, extent and climatic conditions of paleoglaciations. The evolution of regional paleoglaciations, which are a proxy for the record of regional climate change (Clark et al., 2009), can be reconstructed using precise dating methods such as ^{10}Be, radiocarbon (^{14}C), optically stimulated luminescence (OSL), and electron spin resonance (ESR). Although a series of glacial deposits is dated in the study area (Fig. 6 and supplementary Table 3), the onset of the last deglaciation still remains controversial (Schäfer et al., 2002; Owen et al., 2003, 2005; Zhou et al., 2005; Kong et al., 2009; Xu and Zhou, 2009; Heyman et al., 2011; Fu et al., 2013; Zhang et al., 2015). These previous data (Fig. 6a) from Ganzi (Chevalier et al., 2017), Litang (Schäfer et al., 2002; Graf et al., 2008; Fu et al., 2013), Daocheng (Xu et al., 2004; Wang et al., 2006; Graf et al., 2008; Xu and Zhou, 2009; Fu et al., 2013; Zhang et al., 2015), Queer mountain (Xu et al., 2010; Zhang et al., 2012; Ou et al., 2013, 2014), and Kangding (Tschudi et al., 2003; Strasky et al., 2009; Yan and Lin, 2017; Bai et al., 2018) provide evidence of two conspicuous glacial advances: one during the Heinrich event 1 (H1) (Heinrich, 1988) at about 16,800 yr (Hemming, 2004, and references therein) and the other one during the Younger Dryas (YD) from 12,823 ± 60 yr to 11,473 ± 100 yr (Wang et al., 2001). In our study, the exposure age of ZGN-7 (~16.6 ka) indicates that sediments were abandoned in the valleys and basins after the LGM (Fig. 7b). Then, the age of ~13.4 ka (XSH-4) corresponds to the period between the H1 and YD glacial advances (Fig. 7a and b). Subsequently, the exposure age of XSH-2 (~5.9 ka) and XSH-3 (~4.0 ka) are consistent with the interval of monsoonal Himalayan-

Tibetan stages (MOHITS) (Murari et al., 2014) or mid-Holocene climate optimum (Fig. 7b). The spatial and temporal distributions of published exposure or burial ages in the eastern Tibetan Plateau are presented in Fig. 6. We obtain an exposure age for the granitic regolith located in the Yidun terrane older than 19.4 ka (unconstrained) or $27.0^{+9.6}_{-7.6}$ ka (with a net erosion less than 100 cm), which indicates that an erosive event occurred in this area approximately 20 ka ago, coincident with global Late Glacial Maximum (e.g., Clark et al., 2009), likely resulting from glacial or periglacial processes. This age is consistent with the presence of the palaeo-Daocheng ice cap during the LGM (Xu and Zhou, 2009; Fu et al., 2013; Zhang et al., 2015). This age is also found as a peak in the age distribution of Fig. 6c, indicating a regional event, and likely related to the glacial to interglacial transition at the end of the LGM. The profile shows inheritance within the regolith, which can be interpreted as proposed in other geographical contexts (e.g., Ackerer et al., 2016) as an evidence of a complex erosive history of the regolith marked by other intense glacial erosive events, prior to the erosive event at 20 ka. In addition, most basin-wide denudation rate data in the eastern Tibetan Plateau are lower than 130 mm/ka (47%, n = 90) (Fig. 6b) and thus, consistently with the regolith denudation rate (lower than 52.8 mm/ka), indicate that the denudation of the landscape is demonstrably stable following the last deglaciation.

5.3. The framework for the late Quaternary fluvial incision in the eastern Tibetan Plateau

The observation of variable incision rates provides insight into the topographic and geomorphic evolution. Previous studies focused on the onset of incision and paid less attention to the variation of the incision rates after the incision began (Kirby et al., 2002; Clark et al., 2005; Godard et al., 2009; Pan et al., 2009; Ouimet et al., 2010; Perrineau et al., 2011). Fluvial incision rates, assumed to be in equilibrium with external forcings over a wide range of timescales especially in a tectonically rising landscape, were commonly interpreted as a proxy for the quantification of tectonic uplift rate and indicating the strength of climate change under the assumption of steady-state (Burbank et al., 1996; Maddy et al., 2000; Kong et al., 2009; Pan et al., 2009; Huang et al., 2014; Ruszkiczay-Rüdiger et al., 2016; Delmas et al., 2018). However, the significant effect of lag time (Fig. 8) between uplift and incision indicates that the river incision becomes periodically negligible in hyper-arid conditions or due to very low gravel flux (Whipple, 2004; Ouimet et al., 2010). In addition, the fluvial incision rate is exaggerated due to the fact that long episodic incision hiatuses, including river bed aggradation and return to pre-deposition (Fig. 8), are ignored (Gardner et al., 1987; Mills, 2000; Schumer and Jerolmack, 2009; Lague, 2010; Finnegan et al., 2014; Zhang et al., 2018). Fig. 8 shows a fluvial incision model to account for the relationship among fluvial incision, tectonic uplift and climate change at different timescales. Exaggerated fluvial incision rates at short timescale are seemingly caused by ignoring the hysteresis effect (e.g., Whipple and Tucker, 2002; Ouimet et al., 2010) and/or episodic hiatuses (e.g., Finnegan et al., 2014) (Fig. 8). The negative power-law dependence of bedrock river incision rate on different timescales (e.g., Schumer and Jerolmack, 2009) is used to interpret that the slopes (green and red dashed line in Fig. 8) decrease with increasing timescale.

On the long timescale of several million years, previous studies using multiple thermochronology methods suggest that the eastern margin of the Tibetan Plateau, including Minjiang, Dadu, Yalong, and Jinsha rivers, experienced high exhumation rates on the order of 0.2–1.0 mm/yr (e.g., Kirby et al., 2002; Clark et al., 2005; Godard et al., 2009; Ouimet et al., 2010; Tian et al., 2018) with initiation ages of ca. 8–15 Ma. Liu et al. (2006) and Zhao et al.
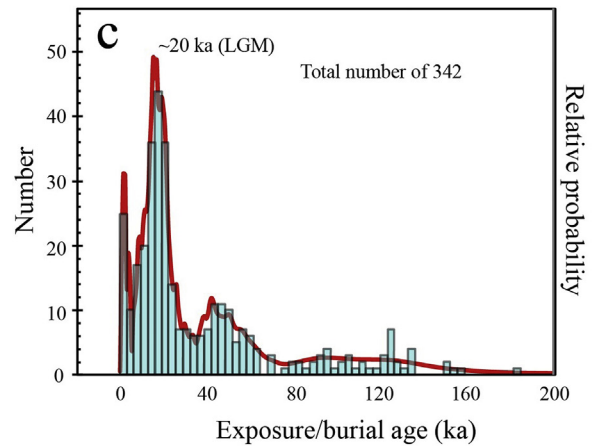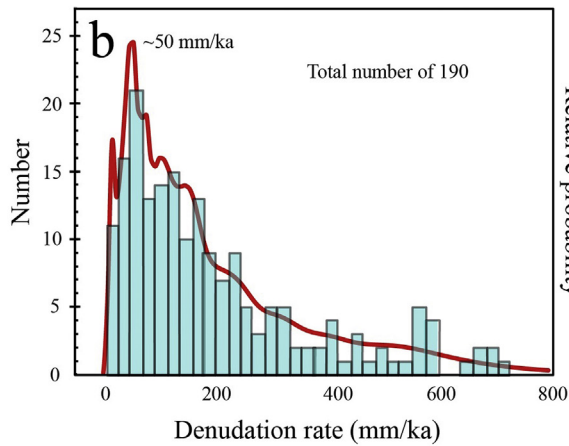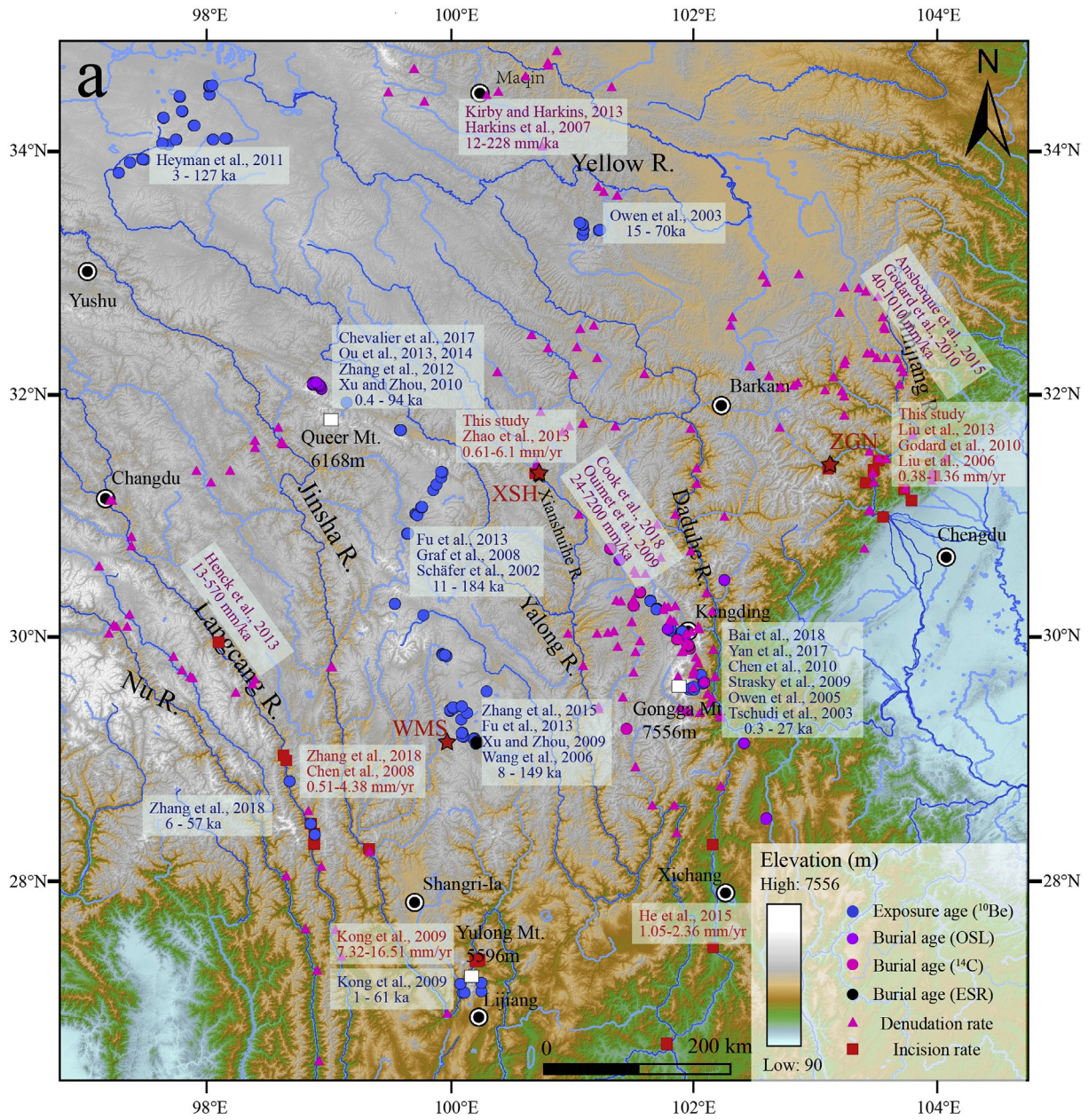
Fig. 6. (a) Spatial distribution of previous exposure/burial ages (circle), basin-wide denudation rates (triangle), and fluvial incision rates (square) over eastern Tibetan Plateau (data in Supplementary Tables 3—5). (b) Distribution of basin-wide denudation rates for modern river sediments. We excluded 18 outliers greater than 800 mm/ka (data in Supplementary Table 3). (c) Distribution of exposure and burial ages (data in Supplementary Table 4). Red curve represents relative probability density function with 1σ error. (For interpretation of the references to color in this figure legend, the reader is referred to the Web version of this article.)
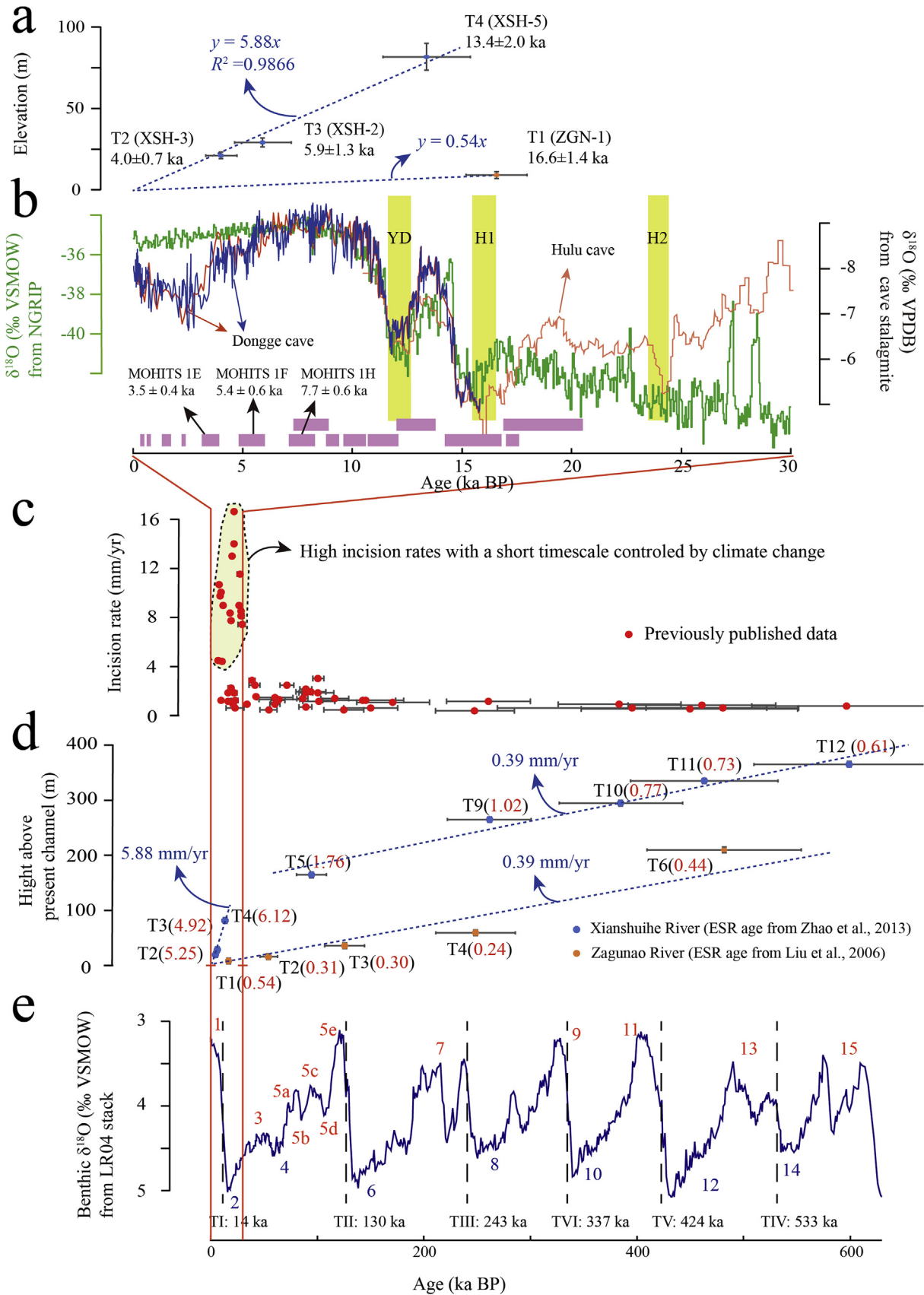
Fig. 7. Comparison of fluvial terraces abandonment ages with b) paleoclimatic records from North Greenland Ice Core Project (NGRIP) oxygen isotope record (North Greenland Ice Core Project et al., 2004), Hulu cave stalagmites oxygen isotope record (Wang et al., 2001), Dongge cave stalagmites oxygen isotope record (Yuan et al., 2004; Dykoski et al., 2005), and e) stacked Benthic oxygen isotope curve (Lisiecki and Raymo, 2005). Blue dashed lines in (a) and (d) show linear relationship between terrace elevations and abandonment ages at different timescales. Yellow bands in (b) indicate timing and duration of Younger Dryas (YD) and Heinrich events 1 and 2 (H1 and H2) (Bond et al., 1993; Hemming, 2004). Purple bands in (b) represent continuous glaciation termed monsoonal Himalayan-Tibetan stages (MOHITS) from MOHITS 1A to MOHITS 2D (Murari et al., 2014). Previous data in (c) are presented in Supplementary Table 5. ESR ages of Xianshuihe and Zagunao rivers are from Zhao et al. (2013) and Liu et al. (2006), respectively. Red numbers in (d) represent average incision rate from formation of terrace to present. (For interpretation of the references to color in this figure legend, the reader is referred to the Web version of this article.)
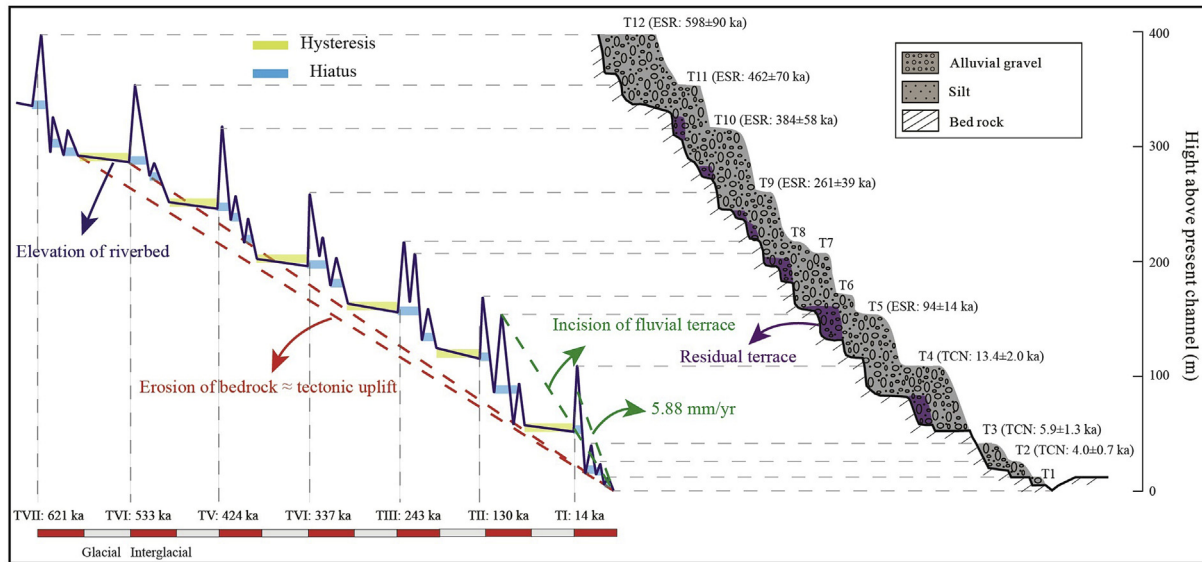
Fig. 8. Simplified model to illustrate river bed evolution of Xianshuihe river and relationship between bedrock erosion, fluvial incision and terrace formation and abandonment. Yellow bars show lag time between uplift and incision, when river incision is periodically cancelled during hyper-arid conditions or low sediment discharge (e.g., Whipple, 2004; Ouimet et al., 2010). Blue bars show episodic incision hiatuses, including river bed aggradation and return to pre-deposition (e.g., Finnegan et al., 2014). TCN and ESR ages are from this study and Zhao et al. (2013), respectively. (For interpretation of the references to color in this figure legend, the reader is referred to the Web version of this article.)

(2013) propose that the Zagunao and Xianhuihe rivers experience a relative stable average incision rate of ~0.39 mm/yr over a long timescale (~600 ka) by using the ESR dating method (Fig. 7d). Similar results of 0.5—0.8 mm/yr are obtained from river watershed-averaged denudation rates along the Longmenshan range front by using the river sediment load data (Liu-Zeng et al., 2011). The consistency between these rates, representative of long-term processes seemingly shows that the incision rate is a proxy for the tectonic uplift rate. But, fluvial incision rates are not strictly equal to the tectonic uplift rates in all circumstances (Gallen et al., 2015), especially at short timescale. An increase incision rate from 1.32 ± 0.37 mm/yr (59.8 ± 16.9 ka) to 4.25 ± 0.76 mm/yr (10.6 ± 1.9 ka) is obtained in the Jinsha fluvial terraces by using the OSL dating method (Chen et al., 2008b). [14]C, OSL, and [10]Be data from terraces in the frontal region of the Longmenshan show that the erosion rate is less than 0.5 ± 0.1 mm/yr (at the timescale of 150 ± 25 ka) and increases to ~1 mm/yr (at the timescale of 20—40 ka) towards the west (Fig. 6a) (Godard et al., 2010). He et al. (2015) also proposed an increase of the incision rate at the timescale of ~60 ka in the lower reach of the Yalong river (Fig. 6a). In our study, a fast incision rate of ~5.88 mm/yr for the last ~10 ka along the Xian-shuihe river contrasts with the long-term incision rate of ~0.39 mm/yr. The compilation of previously reported fluvial incision rates (see detail in supplementary Table 5) shows a peak of fast incision rates at the short timescale of ~10 ka in the eastern Tibetan Plateau (Fig. 7c). Our results show that the fluvial incision rate varies by at least one order of magnitude depending on the time scale of observation (Figs. 6 and 7), implying decoupling between regional long-term landscape erosion rates and fluvial incision (e.g., Zhang et al., 2018). The slight increase of incision rate along the Zagunao river may be due to its lower altitude, less frost shattering and denser vegetation. According to the published data and our cosmogenic [10]Be and [26]Al results, we propose that the fluvial incision rate is mainly influenced by the abrupt climate change or the intensified summer monsoon in the eastern Tibetan Plateau since the early Holocene (Chen et al., 2008a), and controlled by tectonic uplift or progressive fluvial headward retreat for longer timescales. These results emphasize the need of the integration of

data at several time scales to unravel the dynamic of river incision and the role of the different processes operating at different time scales (e.g., Mills, 2000; Whipple and Tucker, 2002; Finnegan et al., 2014; Zhang et al., 2018).

5.4. An integrated driving mechanisms of landscape evolution in the eastern Tibetan Plateau

The competition between fluvial incision processes and tectonic uplift processes is generally considered for the topographic and geomorphic evolution of mountain belts (e.g., Burbank et al., 1996; Maddy et al., 2000; Pan et al., 2009; Ruszkiczay-Rüdiger et al., 2016). In addition, the formation of fluvial terraces is mainly controlled by the synergistic effects of fluvial incision, tectonic uplift and climate change (e.g., Bull, 1991; Hancock and Anderson, 2002). However, quantifying the contributions of climate change and tectonic uplift from river incision rates is not straightforward. The great changes of flood magnitude and frequency caused by the climatic transitions are responsible for the formation of fluvial terraces (e.g., Chen et al., 2008b; Huang et al., 2014; He et al., 2015; Delmas et al., 2018; Zhang et al., 2018). During glacial periods, enhanced frost shattering and degradation of vegetation both caused an excess of sediment (on the slopes). Subsequently, these large amounts of sediments are transported in basins or valleys when the climate becomes warmer and wetter during interglacial, which is coupled to the erosive event that occurred on the bedrock surface of Wumingshan regolith (see detail in section 5.2). Because of reworking and/or recycling of the sediment not all glacial-interglacial transitions remain in the terrace record (purple shaded area in Fig. 8) (e.g., Cogez et al., 2018). Fluvial terraces emplaced during previous glacial terminations, as the last seven glacial terminations (Lisiecki and Raymo, 2005), are most probably reworked or recycled by subsequent glacial-interglacial transitions (Fig. 8). On the long-term, crustal isostatic rebound caused by the unloading as a result of deglaciation (e.g., Rohling et al., 2017) and surface erosion/denudation processes (e.g., Burbank, 1992; Kirby et al., 2000) cannot be ignored (Whipple, 2009; Molnar, 2012). The information of fluvial incision has been recorded and its

acceleration during the Holocene is likely the consequence of several processes: (i) the long-term tectonic uplift together with fluvial headward erosion; (ii) the short-term dramatic climate change at glacial-interglacial transitions; and (iii) the long-term isostatic rebound caused by the unloading as a result of deglaciation and surface denudation processes.

6. Conclusions

An integrated analysis of last deglaciation, local denudation and fluvial incision leads to the evaluation of landscape evolution, climate change and tectonic uplift in the eastern Tibetan Plateau. In this study, we obtain the exposure age older than 19.4 ka (or $27.0^{+9.6}_{-7.6}$ ka with constraints) and the denudation rate lower than 52.8 mm/ka (or $18.4^{+14.4}_{-18.4}$ mm/kyr with constraints) (Fig. 5) for the Wumingshan regolith (Yidun pluton) at the eastern margin of the Tibetan Plateau. These results coincide with the timing of the last deglaciation and reveal a stable landscape after the glacial or periglacial erosive event in this area. Our fluvial incision rates inferred from terrace ages, associated to previous river incision data show that the present fluvial incision rate is mainly influenced by the abrupt climate change or the intensified summer monsoon in the eastern Tibetan Plateau since the early Holocene, and that long-term incision rates are probably linked to tectonic uplift or fluvial headward retreat. The driving mechanisms of accelerated fluvial incision rate during the late Quaternary is interpreted as the synthetic pattern of landscape evolution mainly dominated by long-term tectonic uplift, periodically influenced by the climatic change and isostasy throughout the late Quaternary.

Appendix A. The three-dimensional-graph visualization approach

According to the inequality derived by different confidence level of $\chi^2 < \chi^2_{2\sigma}$, $\chi^2 < \chi^2_{1\sigma}$ or $\chi^2 < \chi^2_{min} + 1$, one or more shaded area representing all the possible solutions were yielded in the three-dimensional space (Figs. A.1a and b). After a reliable constraint, the plot range of denudation rate, exposure age, and inheritance need to be adjusted so that the black points almost fill the three-dimensional space (Fig. A.1a, the inset box shows the plot range of Fig. A.1b). We use the method of Rodés et al. (2011) and Braucher

et al. (2009) to generate a denudation-age-inheritance space. The greater the number of points (can be adjusted by the increments) in the shaded area, the higher the accuracy of the analysis. In addition, it is a time-consuming process to yield a better statistical analysis accuracy. Statistical analysis for all possible solutions in the orange shaded area (Fig. A.1b), which represents a confidence level of $\chi^2_{min} + 1$, can yield the minimum, maximum, mean, mode, and median solutions of denudation rate, exposure age, and inheritance, respectively (supplementary Table 1). Figs. A.1c, d and e show the χ^2 plots for denudation rate, exposure age, and inheritance values, and the inset diagrams show the probability distribution functions (PDFs) and cumulative distribution functions (CDFs) for denudation rate, exposure age, and inheritance, respectively.

Appendix B. Constraint on the variable-density approach

In order to model the complex geological process of the accumulated loess, we combine the method of Charreau et al. (2017) and the variable-density approach. The mean age and two end-member ages have been estimated from the modeling as follows:

Model 1: instantaneous deposition

If we consider that the loess was instantaneously deposited after terrace abandonment and subsequently experienced a constant denudation ($\varepsilon > 0$) (Fig. B.1a), the three free parameters (denudation rate, exposure age, and inheritance), described by Equation (3), are determined by the 3D-graph visualization approach.

Model 2: continuous deposition

Continuous deposition at a constant accumulation rate ($\varepsilon < 0$) after terrace abandonment has been assumed to get the mean age (Fig. B.1b). In addition, the exposure age and accumulation rate are dependent on the total depth of loess ($x_{loess} = -\varepsilon \times t$). Then, Equation (3) becomes:

$$C(x, \varepsilon, t) = c_0 e^{-\lambda t} + \sum_{i=spal,slow,fast} \frac{P_i}{\lambda - \frac{\rho_{loess} x_{loess}}{\Lambda_i t}} e^{-\left(\frac{\rho_{xsed} x_{sed} + \rho_{loess} x_{loess}}{\Lambda_i} \right)}$$
$$\left[1 - e^{-\left(\lambda t - \frac{\rho_{loess} x_{loess}}{\Lambda_i} \right)} \right]$$

$$(B.1)$$

In this case, the total depth of loess was used to constrain the 3D-graph visualization approach. Two free parameters (exposure age and inheritance) were determined by the previous method (Siame et al., 2004; Rodés et al., 2011).

Model 3: Very recent deposition

In order to get the minimum end-member age, we assume the profile experienced a constant denudation before the very recent deposition of loess (Fig. B.1c). The 3D-graph visualization approach with no variation of density was used to determine denudation rate, exposure age and inheritance.
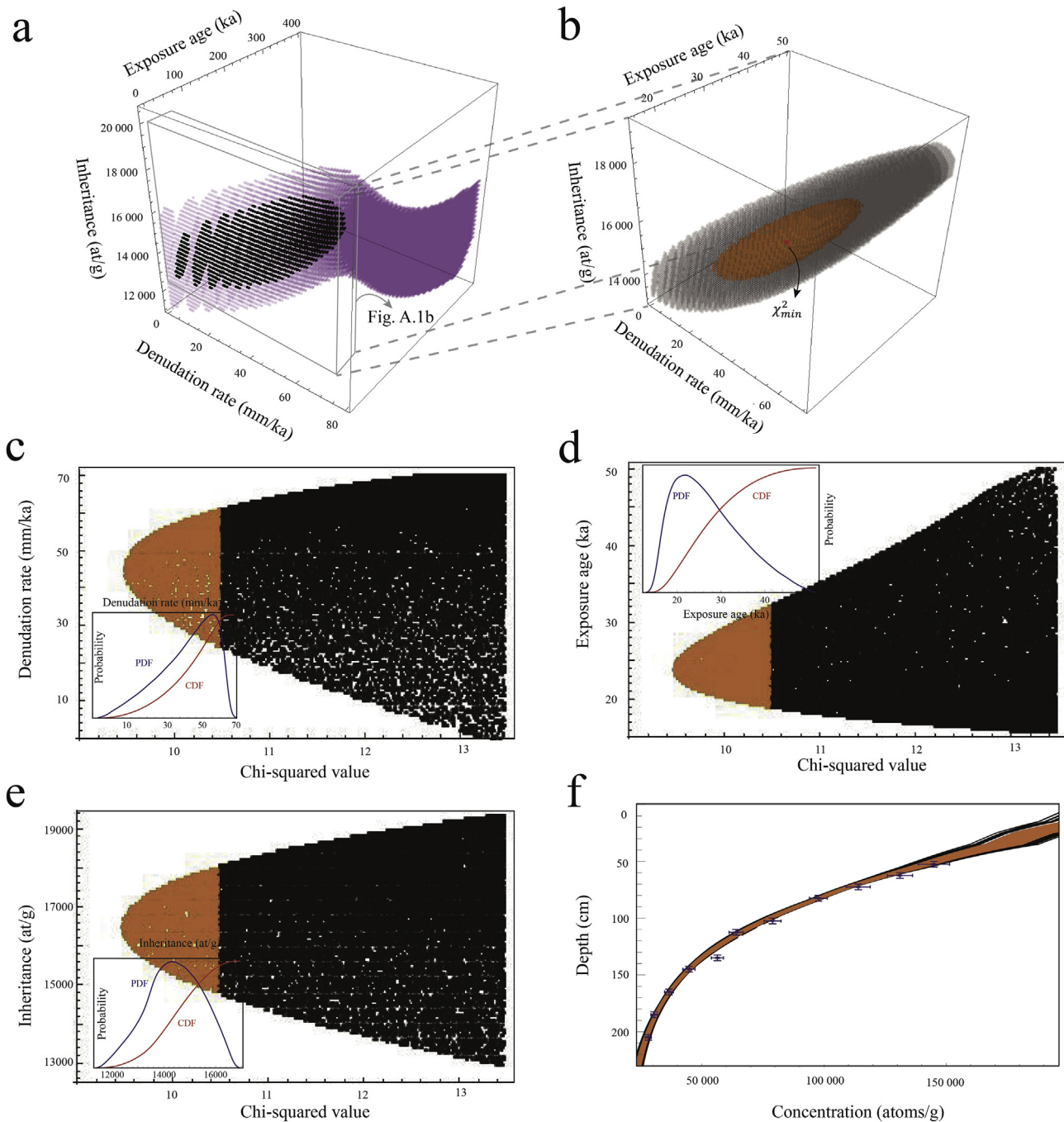
Fig. A.1. Three-dimensional-graph visualization approach and statistical analysis of possible solutions. Data from Ackerer et al. (2016). (a) purple and black points represent possible solutions within 2σ and 1σ confidence levels, respectively; (b) black and orange points represent possible solutions within 1σ confidence level and $\chi^2_{min} + 1$, respectively (see detail in Appendix A); (c-e) χ^2 value plots for denudation rate, exposure age and inheritance, in addition, inset diagrams show probability distribution functions (PDFs) and cumulative distribution functions (CDFs); (f) Cosmogenic nuclide concentration as a function of depth for possible solutions within confidence level.
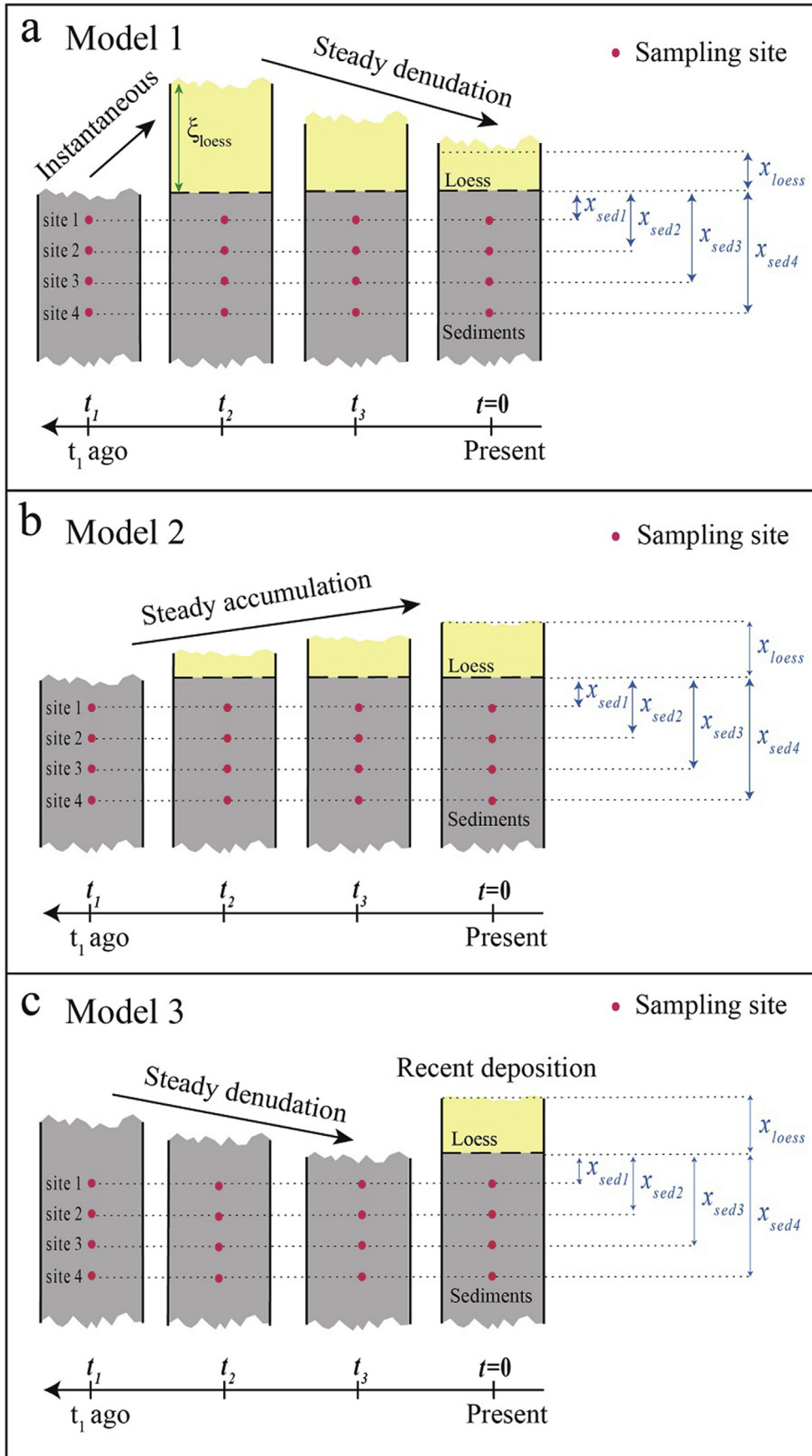
Fig. B.1. Schematic diagrams illustrate variable-density approach with three different loess cover models. (a) Model 1: instantaneous loess deposition after terrace abandonment and post-deposition constant denudation; (b) Model 2: continuous loess deposition at a constant accumulation rate after terrace abandonment; (c) Model 3: experience a constant denudation of terrace before very recent loess deposition event.

Appendix C. Supplementary data

Supplementary data to this article can be found online at https://doi.org/10.1016/j.quascirev.2019.07.020.

References

Ackerer, J., Chabaux, F., Van der Woerd, J., Viville, D., Pelt, E., Kali, E., Lerouge, C., Ackerer, P., di Chiara Roupert, R., Négrel, P., 2016. Regolith evolution on the millennial timescale from combined U–Th–Ra isotopes and in situ cosmogenic [10]Be analysis in a weathering profile (Strengbach catchment, France). Earth Planet. Sci. Lett. 453, 33–43.

Akçar, N., Ivy-Ochs, S., Alfimov, V., Schlunegger, F., Claude, A., Reber, R., Christl, M., Vockenhuber, C., Dehnert, A., Rahn, M., Schlüchter, C., 2017. Isochron-burial dating of glaciofluvial deposits: first results from the Swiss Alps. Earth Surf. Process. Landforms 42, 2414–2425.

Ansberque, C., Godard, V., Bellier, O., De Sigoyer, J., Liu-Zeng, J., Xu, X., Ren, Z., Li, Y., Team, A.S.T.E.R., 2015. Denudation pattern across the Longriba fault system and implications for the geomorphological evolution of the eastern Tibetan margin. Geomorphology 246, 542–557.

Arnold, M., Merchel, S., Bourlès, D.L., Braucher, R., Benedetti, L., Finkel, R.C., Aumaître, G., Gottdang, A., Klein, M., 2010. The French accelerator mass spectrometry facility ASTER: improved performance and developments. Nucl. Instrum. Methods Phys. Res. Sect. B Beam Interact. Mater. Atoms 268, 1954–1959.

Aster, R.C., Borchers, B., Thurber, C.H., 2013. Parameter Estimation and Inverse Problems, second ed. Academic Press, Amsterdam.

Bai, M., Chevalier, M.-L., Pan, J., Replumaz, A., Leloup, P.H., Métois, M., Li, H., 2018. Southeastward increase of the late Quaternary slip-rate of the Xianshuihe fault, eastern Tibet. Geodynamic and seismic hazard implications. Earth Planet. Sci. Lett. 485, 19–31.

Balco, G., 2017. Production rate calculations for cosmic-ray-muon-produced [10]Be and [26]Al benchmarked against geological calibration data. Quat. Geochronol. 39, 150–173.

Balco, G., Stone, J.O., Lifton, N.A., Dunai, T.J., 2008. A complete and easily accessible means of calculating surface exposure ages or erosion rates from [10]Be and [26]Al measurements. Quat. Geochronol. 3, 174–195.

Bevington, P.R., Robinson, D.K., 2003. Data Reduction and Error Analysis for the Physical Sciences. McGraw-Hill higher Education, New York.

Bond, G., Broecker, W., Johnsen, S., McManus, J., Labeyrie, L., Jouzel, J., Bonani, G., 1993. Correlations between climate records from North Atlantic sediments and Greenland ice. Nature 365, 143.

Bookhagen, B., 2018. High Resolution Spatiotemporal Distribution of Rainfall Seasonality and Extreme Events Based on a 12-year TRMM Time Series. In Review.

Borchers, B., Marrero, S., Balco, G., Caffee, M., Goehring, B., Lifton, N., Nishiizumi, K., Phillips, F., Schaefer, J., Stone, J., 2016. Geological calibration of spallation production rates in the CRONUS-Earth project. Quat. Geochronol. 31, 188–198.

Braucher, R., Bourlès, D., Merchel, S., Vidal Romani, J., Fernadez-Mosquera, D., Marti, K., Léanni, L., Chauvet, F., Arnold, M., Aumaître, G., Keddadouche, K., 2013. Determination of muon attenuation lengths in depth profiles from in situ produced cosmogenic nuclides. Nucl. Instrum. Methods Phys. Res. Sect. B Beam Interact. Mater. Atoms 294, 484–490.

Braucher, R., Brown, E.T., Bourlès, D.L., Colin, F., 2003. In situ produced [10]Be measurements at great depths: implications for production rates by fast muons. Earth Planet. Sci. Lett. 211, 251–258.

Braucher, R., Del Castillo, P., Siame, L., Hidy, A.J., Bourlès, D.L., 2009. Determination of both exposure time and denudation rate from an in situ-produced [10]Be depth profile: a mathematical proof of uniqueness. Model sensitivity and applications to natural cases. Quat. Geochronol. 4, 56–67.

Braucher, R., Guillou, V., Bourlès, D.L., Arnold, M., Aumaître, G., Keddadouche, K., Nottoli, E., 2015. Preparation of ASTER in-house [10]Be/[9]Be standard solutions. Nucl. Instrum. Methods Phys. Res. Sect. B Beam Interact. Mater. Atoms 361, 335–340.

Braucher, R., Merchel, S., Borgomano, J., Bourlès, D.L., 2011. Production of cosmogenic radionuclides at great depth: a multi element approach. Earth Planet. Sci. Lett. 309, 1–9.

Bull, W.B., 1991. Geomorphic Responses to Climatic Change. Oxford University Press, New York.

Burbank, D.W., 1992. Causes of recent Himalayan uplift deduced from deposited patterns in the Ganges basin. Nature 357, 680–683.

Burbank, D.W., Leland, J., Fielding, E., Anderson, R.S., 1996. Bedrock incision, rock uplift and threshold hillslopes in the northwestern Himalayas. Nature 379, 505.

Burchfiel, B.C., Chen, Z., Liu, Y., Royden, L.H., 1995. Tectonics of the Longmen Shan and adjacent regions, Central China. Int. Geol. Rev. 37, 661–735.

Carretier, S., Regard, V., Vassallo, R., Aguilar, G., Martinod, J., Riquelme, R., Christophoul, F., Charrier, R., Gayer, E., Farías, M., Audin, L., Lagane, C., 2015. Differences in [10]Be concentrations between river sand, gravel and pebbles along the western side of the central Andes. Quat. Geochronol. 27, 33–51.

Charreau, J., Saint-Carlier, D., Dominguez, S., Lavé, J., Blard, P.-H., Avouac, J.-P., Jolivet, M., Chen, Y., Wang, S., Brown, N.D., Malatesta, L.C., Rhodes, E., 2017. Denudation outpaced by crustal thickening in the eastern Tianshan. Earth Planet. Sci. Lett. 479, 179–191.

Chen, F., Yu, Z., Yang, M., Ito, E., Wang, S., Madsen, D.B., Huang, X., Zhao, Y., Sato, T., John, B., Birks, H., Boomer, I., Chen, J., An, C., Wünnemann, B., 2008a. Holocene

moisture evolution in arid central Asia and its out-of-phase relationship with Asian monsoon history. Quat. Sci. Rev. 27, 351–364.

Chen, J., Dai, F., Yao, X., 2008b. Holocene debris-flow deposits and their implications on the climate in the upper Jinsha River valley, China. Geomorphology 93, 493–500.

Chevalier, M.-L., Leloup, P.H., Replumaz, A., Pan, J., Métois, M., Li, H., 2017. Temporally constant slip rate along the Ganzi fault, NW Xianshuihe fault system, eastern Tibet. Geol. Soc. Am. Bull. 130, 396–410.

Chmeleff, J., von Blanckenburg, F., Kossert, K., Jakob, D., 2010. Determination of the [10]Be half-life by multicollector ICP-MS and liquid scintillation counting. Nucl. Instrum. Methods Phys. Res. Sect. B Beam Interact. Mater. Atoms 268, 192–199.

Clark, M.K., House, M.A., Royden, L.H., Whipple, K.X., Burchfiel, B.C., Zhang, X., Tang, W., 2005. Late Cenozoic uplift of southeastern Tibet. Geology 33, 525.

Clark, M.K., Royden, L.H., 2000. Topographic ooze: building the eastern margin of Tibet by lower crustal flow. Geology 28, 703–706.

Clark, M.K., Royden, L.H., Whipple, K.X., Burchfiel, B.C., Zhang, X., Tang, W., 2006. Use of a regional, relict landscape to measure vertical deformation of the eastern Tibetan Plateau. J. Geophys. Res. Earth Surf. 111, F03002.

Clark, M.K., Schoenbohm, L.M., Royden, L.H., Whipple, K.X., Burchfiel, B.C., Zhang, X., Tang, W., Wang, E., Chen, L., 2004. Surface uplift, tectonics, and erosion of eastern Tibet from large-scale drainage patterns. Tectonics 23, TC1006.

Clark, P.U., Dyke, A.S., Shakun, J.D., Carlson, A.E., Clark, J., Wohlfarth, B., Mitrovica, J.X., Hostetler, S.W., McCabe, A.M., 2009. The last glacial maximum. Science 325, 710–714.

Codilean, A.T., Fenton, C.R., Fabel, D., Bishop, P., Xu, S., 2014. Discordance between cosmogenic nuclide concentrations in amalgamated sands and individual fluvial pebbles in an arid zone catchment. Quat. Geochronol. 19, 173–180.

Cogez, A., Herman, F., Pelt, É., Reuschlé, T., Morvan, G., Darvill, C.M., Norton, K.P., Christl, M., Märki, L., Chabaux, F., 2018. U–Th and [10]Be constraints on sediment recycling in proglacial settings, Lago Buenos Aires, Patagonia. Earth Surf. Dyn. 6, 121–140.

Cui, L.F., Liu, C.Q., Xu, S., Zhao, Z.Q., Liu, T.Z., Liu, W.J., Zhang, Z.J., 2016. Subtropical denudation rates of granitic regolith along a hill ridge in Longnan, SE China derived from cosmogenic nuclide depth-profiles. J. Asian Earth Sci. 117, 146–152.

Cui, L.F., Liu, C.Q., Xu, S., Zhao, Z.Q., Tu, C.L., Liu, T.Z., Ding, H., 2014. The long-term denudation rate of granitic regolith in Qinhuangdao, North China determined from the in situ depth profile of the cosmogenic nuclides [26]Al and [10]Be. Chin. Sci. Bull. 59, 4823–4828.

Delmas, M., Calvet, M., Gunnell, Y., Voinchet, P., Manel, C., Braucher, R., Tissoux, H., Bahain, J.-J., Perrenoud, C., Saos, T., 2018. Terrestrial [10]Be and electron spin resonance dating of fluvial terraces quantifies Quaternary tectonic uplift gradients in the eastern Pyrenees. Quat. Sci. Rev. 193, 188–211.

Dykoski, C., Edwards, R., Cheng, H., Yuan, D., Cai, Y., Zhang, M., Lin, Y., Qing, J., An, Z., Revenaugh, J., 2005. A high-resolution, absolute-dated Holocene and deglacial Asian monsoon record from Dongge Cave, China. Earth Planet. Sci. Lett. 233, 71–86.

Finnegan, N.J., Schumer, R., Finnegan, S., 2014. A signature of transience in bedrock river incision rates over timescales of 10^4-10^7 years. Nature 505, 391–394.

Fu, P., Stroeven, A.P., Harbor, J.M., Hättestrand, C., Heyman, J., Caffee, M.W., Zhou, L., 2013. Paleoglaciation of Shaluli Shan, southeastern Tibetan plateau. Quat. Sci. Rev. 64, 121–135.

Gallen, S.F., Pazzaglia, F.J., Wegmann, K.W., Pederson, J.L., Gardner, T.W., 2015. The dynamic reference frame of rivers and apparent transience in incision rates. Geology 43, 623–626.

Gao, Y.X., 1962. On some problems of Asian monsoon. In: Gao, Y.X. (Ed.), Some Problems on East-Asia Monsoon. Science Press, Beijing, pp. 49–63 (in Chinese).

Gardner, T.W., Jorgensen, D.W., Shuman, C., Lemieux, C.R., 1987. Geomorphic and tectonic process rates: effects of measured time interval. Geology 15, 259–261.

Godard, V., Lavé, J., Carcaillet, J., Cattin, R., Bourlès, D., Zhu, J., 2010. Spatial distribution of denudation in Eastern Tibet and regressive erosion of plateau margins. Tectonophysics 491, 253–274.

Godard, V., Pik, R., Lavé, J., Cattin, R., Tibari, B., de Sigoyer, J., Pubellier, M., Zhu, J., 2009. Late Cenozoic evolution of the central Longmen Shan, eastern Tibet: insight from (U-Th)/He thermochronometry. Tectonics 28, TC5009.

Graf, A.A., Strasky, S., Zhao, Z., Akcar, N., Ivy-Ochs, S., Kubik, P.W., Christal, M., Kasper, H.U., Wieler, R., Schlüchter, C., 2008. Glacier extension on the eastern Tibetan Plateau in response to MIS 2 cooling, with a contribution to [10]Be and [21]Ne methodology. In: Strasky, S. (Ed.), Glacial Response to Global Climate Changes: Cosmogenic Nuclide Chronologies from High and Low Latitudes. ETH Zürich (PhD Thesis).

Granger, D.E., Smith, A.L., 2000. Dating buried sediments using radioactive decay and muogenic production of [26]Al and [10]Be. Nucl. Instrum. Methods Phys. Res. Sect. B Beam Interact. Mater. Atoms 172, 822–826.

Guilbaud, C., Simoes, M., Barrier, L., Laborde, A., Van der Woerd, J., Li, H., Tapponnier, P., Coudroy, T., Murray, A., 2017. Kinematics of active deformation across the western Kunlun mountain range (Xinjiang, China) and potential seismic hazards within the southern Tarim basin. J. Geophys. Res. Solid Earth 122, 10398–10426.

Guralnik, B., Matmon, A., Avni, Y., Porat, N., Fink, D., 2011. Constraining the evolution of river terraces with integrated OSL and cosmogenic nuclide data. Quat. Geochronol. 6, 22–32.

Hancock, G.S., Anderson, R.S., 2002. Numerical modeling of fluvial strath-terrace formation in response to oscillating climate. Geol. Soc. Am. Bull. 114, 1131–1142.

Hancock, G.S., Anderson, R.S., Chadwick, O.A., Finkel, R.C., 1999. Dating fluvial

terraces with [10]Be and [26]Al profiles: application to the wind river, Wyoming. Geomorphology 27, 41—60.

He, Z., Zhang, X., Qiao, Y., Bao, S., Lu, C., He, X., 2015. formation of the Yalong downstream terraces in the SE Tibetan plateau and its implication for the uplift of the plateau. Acta Geol. Sin. (Engl. Ed.) 89, 542—560.

Heinrich, H., 1988. Origin and consequences of cyclic ice rafting in the Northeast Atlantic Ocean during the past 130,000 years. Quat. Res. 29, 142—152.

Hemming, S.R., 2004. Heinrich events: massive late Pleistocene detritus layers of the North Atlantic and their global climate imprint. Rev. Geophys. 42, RG1005.

Heyman, J., Stroeven, A.P., Caffee, M.W., Hättestrand, C., Harbor, J.M., Li, Y., Alexanderson, H., Zhou, L., Hubbard, A., 2011. Palaeoglaciology of Bayan Har Shan, NE Tibetan Plateau: exposure ages reveal a missing LGM expansion. Quat. Sci. Rev. 30, 1988—2001.

Hidy, A.J., Gosse, J.C., Pederson, J.L., Mattern, J.P., Finkel, R.C., 2010. A geologically constrained Monte Carlo approach to modeling exposure ages from profiles of cosmogenic nuclides: an example from Lees Ferry, Arizona. Geochem. Geophys. Geosyst. 11, Q0AA10.

Hidy, A.J., Gosse, J.C., Sanborn, P., Froese, D.G., 2018. Age-erosion constraints on an Early Pleistocene paleosol in Yukon, Canada, with profiles of [10]Be and [26]Al: evidence for a significant loess cover effect on cosmogenic nuclide production rates. Catena 165, 260—271.

Hu, P., Liu, Q., Heslop, D., Roberts, A.P., Jin, C., 2015. Soil moisture balance and magnetic enhancement in loess—paleosol sequences from the Tibetan Plateau and Chinese Loess Plateau. Earth Planet. Sci. Lett. 409, 120—132.

Huang, W.-L., Yang, X.-p., Li, A., Thompson, J.A., Zhang, L., 2014. Climatically controlled formation of river terraces in a tectonically active region along the southern piedmont of the Tian Shan, NW China. Geomorphology 220, 15—29.

Kirby, E., Reiners, P.W., Krol, M.A., Whipple, K.X., Hodges, K.V., Farley, K.A., Tang, W., Chen, Z., 2002. Late Cenozoic evolution of the eastern margin of the Tibetan Plateau: inferences from [40]Ar/[39]Ar and (U - Th)/He thermochronology. Tectonics 21, 1—20.

Kirby, E., Whipple, K.X., Burchfiel, B.C., Tang, W., Berger, G., Sun, Z., Chen, Z., 2000. Neotectonics of the Min Shan, China: implications for mechanisms driving Quaternary deformation along the eastern margin of the Tibetan Plateau. Geol. Soc. Am. Bull. 112, 375—393.

Kong, P., Na, C., Fink, D., Zhao, X., Xiao, W., 2009. Moraine dam related to late Quaternary glaciation in the Yulong Mountains, southwest China, and impacts on the Jinsha River. Quat. Sci. Rev. 28, 3224—3235.

Korschinek, G., Bergmaier, A., Faestermann, T., Gerstmann, U.C., Knie, K., Rugel, G., Wallner, A., Dillmann, I., Dollinger, G., von Gostomski, C.L., Kossert, K., Maiti, M., Poutivtsev, M., Remmert, A., 2010. A new value for the half-life of [10]Be by Heavy-Ion Elastic Recoil Detection and liquid scintillation counting. Nucl. Instrum. Methods Phys. Res. Sect. B Beam Interact. Mater. Atoms 268, 187—191.

Lague, D., 2010. Reduction of long-term bedrock incision efficiency by short-term alluvial cover intermittency. J. Geophys. Res. Earth Surf. 115, F02011.

Lal, D., 1991. Cosmic ray labeling of erosion surfaces: in situ nuclide production rates and erosion models. Earth Planet. Sci. Lett. 104, 424—439.

Lisiecki, L.E., Raymo, M.E., 2005. A Pliocene-Pleistocene stack of 57 globally distributed benthic $\delta^{18}O$ records. Paleoceanography 20, 1—17.

Liu-Zeng, J., Tapponnier, P., Gaudemer, Y., Ding, L., 2008. Quantifying landscape differences across the Tibetan plateau: implications for topographic relief evolution. J. Geophys. Res. 113, F04018.

Liu-Zeng, J., Wen, L., Oskin, M., Zeng, L., 2011. Focused modern denudation of the Longmen Shan margin, eastern Tibetan Plateau. Geochem. Geophys. Geosyst. 12, Q11007.

Liu-Zeng, J., Zhang, J., McPhillips, D., Reiners, P., Wang, W., Pik, R., Zeng, L., Hoke, G., Xie, K., Xiao, P., Zheng, D., Ge, Y., 2018. Multiple episodes of fast exhumation since Cretaceous in southeast Tibet, revealed by low-temperature thermochronology. Earth Planet. Sci. Lett. 490, 62—76.

Liu, J., Chen, J., Zhang, X., Li, Y., Rao, Z., Chen, F., 2015. Holocene East Asian summer monsoon records in northern China and their inconsistency with Chinese stalagmite $\delta^{18}O$ records. Earth Sci. Rev. 148, 194—208.

Liu, Y., Zhao, Z., Li, C., Zhang, M., Chen, Y., 2006. formation of the Zagunao river terraces in western Sichuan plateau, China. Acta Geograph. Sin. 61, 249—254 (in Chinese with English abstract).

Maddy, D., Bridgland, D.R., Green, C.P., 2000. Crustal uplift in southern England: evidence from the river terrace records. Geomorphology 33, 167—181.

Marrero, S.M., Phillips, F.M., Borchers, B., Lifton, N., Aumer, R., Balco, G., 2016. Cosmogenic nuclide systematics and the CRONUScalc program. Quat. Geochronol. 31, 160—187.

Martin, L.C.P., Blard, P.H., Balco, G., Lavé, J., Delunel, R., Lifton, N., Laurent, V., 2017. The CREp program and the ICE-D production rate calibration database: a fully parameterizable and updated online tool to compute cosmic-ray exposure ages. Quat. Geochronol. 38, 25—49.

Maussion, F., Scherer, D., Mölg, T., Collier, E., Curio, J., Finkelnburg, R., 2014. Precipitation seasonality and variability over the Tibetan plateau as resolved by the high Asia reanalysis. J. Clim. 27, 1910—1927.

Métivier, F., Gaudemer, Y., Tapponnier, P., Meyer, B., 1998. Northeastward growth of the Tibet plateau deduced from balanced reconstruction of two depositional areas: the Qaidam and Hexi Corridor basins, China. Tectonics 17, 823—842.

Mills, H.H., 2000. Apparent increasing rates of stream incision in the eastern United States during the late Cenozoic. Geology 28, 955—957.

Molnar, P., 2012. Isostasy can't be ignored. Nat. Geosci. 5, 83.

Molnar, P., Boos, W.R., Battisti, D.S., 2010. Orographic controls on climate and paleoclimate of Asia: Thermal and mechanical roles for the Tibetan plateau. Annu. Rev. Earth Planet Sci. 38, 77—102.

Molnar, P., Brown, E.T., Burchfiel, B.C., Deng, Q., Feng, X., Li, J., Raisbeck, G.M., Shi, J., Zhangming, W., Yiou, F., You, H., 1994. Quaternary climate change and the formation of river terraces across growing anticlines on the north Flank of the tien Shan, China. J. Geol. 102, 583—602.

Murari, M.K., Owen, L.A., Dortch, J.M., Caffee, M.W., Dietsch, C., Fuchs, M., Haneberg, W.C., Sharma, M.C., Townsend-Small, A., 2014. Timing and climatic drivers for glaciation across monsoon-influenced regions of the Himalayan—Tibetan orogen. Quat. Sci. Rev. 88, 159—182.

Nishiizumi, K., 2004. Preparation of [26]Al AMS standards. Nucl. Instrum. Methods Phys. Res. Sect. B Beam Interact. Mater. Atoms 223—224, 388—392.

North Greenland Ice Core Project, M., Andersen, K.K., Azuma, N., Barnola, J.M., Bigler, M., Biscaye, P., Caillon, N., Chappellaz, J., Clausen, H.B., Dahl-Jensen, D., Fischer, H., Flückiger, J., Fritzsche, D., Fujii, Y., Goto-Azuma, K., Grønvold, K., Gundestrup, N.S., Hansson, M., Huber, C., Hvidberg, C.S., Johnsen, S.J., Jonsell, U., Jouzel, J., Kipfstuhl, S., Landais, A., Leuenberger, M., Lorrain, R., Masson-Delmotte, V., Miller, H., Motoyama, H., Narita, H., Popp, T., Rasmussen, S.O., Raynaud, D., Rothlisberger, R., Ruth, U., Samyn, D., Schwander, J., Shoji, H., Siggard-Andersen, M.L., Steffensen, J.P., Stocker, T., Sveinbjörnsdóttir, A.E., Svensson, A., Takata, M., Tison, J.L., Thorsteinsson, T., Watanabe, O., Wilhelms, F., White, J.W.C., 2004. High-resolution record of Northern Hemisphere climate extending into the last interglacial period. Nature 431, 147—151.

Ou, X., Lai, Z., Zhou, S., Zeng, L., 2014. Timing of glacier fluctuations and trigger mechanisms in eastern Qinghai—Tibetan Plateau during the late Quaternary. Quat. Res. 81, 464—475.

Ou, X., Zhang, B., Lai, Z., Zhou, S., Zeng, L., 2013. OSL dating study on the glacial evolutions during the last glaciation at Dangzi valley in the eastern Qinghai-Tibetan plateau. Prog. Geogr. 32, 262—269 (in Chinese with English abstract).

Ouimet, W., Whipple, K., Royden, L., Reiners, P., Hodges, K., Pringle, M., 2010. Regional incision of the eastern margin of the Tibetan Plateau. Lithosphere 2, 50—63.

Owen, L.A., Finkel, R.C., Barnard, P.L., Haizhou, M., Asahi, K., Caffee, M.W., Derbyshire, E., 2005. Climatic and topographic controls on the style and timing of Late Quaternary glaciation throughout Tibet and the Himalaya defined by [10]Be cosmogenic radionuclide surface exposure dating. Quat. Sci. Rev. 24, 1391—1411.

Owen, L.A., Finkel, R.C., Haizhou, M., Spencer, J.Q., Derbyshire, E., Barnard, P.L., Caffee, M.W., 2003. Timing and style of late Quaternary glaciation in northeastern Tibet. Geol. Soc. Am. Bull. 115, 1356—1364.

Pan, B., Su, H., Hu, Z., Hu, X., Gao, H., Li, J., Kirby, E., 2009. Evaluating the role of climate and tectonics during non-steady incision of the Yellow River: evidence from a 1.24 Ma terrace record near Lanzhou, China. Quat. Sci. Rev. 28, 3281—3290.

Perrineau, A., Van der Woerd, J., Gaudemer, Y., Liu-Zeng, J., Pik, R., Tapponnier, P., Thuizat, R., Zheng, R., 2011. Incision rate of the Yellow River in Northeastern Tibet constrained by [10]Be and [26]Al cosmogenic isotope dating of fluvial terraces: implications for catchment evolution and plateau building. Geol. Soc. Lond. Spec. Publ. 353, 189—219.

Phillips, F.M., Argento, D.C., Balco, G., Caffee, M.W., Clem, J., Dunai, T.J., Finkel, R., Goehring, B., Gosse, J.C., Hudson, A.M., Jull, A.J.T., Kelly, M.A., Kurz, M., Lal, D., Lifton, N., Marrero, S.M., Nishiizumi, K., Reedy, R.C., Schaefer, J., Stone, J.O.H., Swanson, T., Zreda, M.G., 2016. The CRONUS-Earth Project: a synthesis. Quat. Geochronol. 31, 119—154.

Qiao, Y., Qi, L., Liu, Z., Wang, Y., Yao, H., Yang, J., Zhao, Z., 2014. Intensification of aridity in the eastern margin of the Tibetan Plateau since 300ka BP inferred from loess-soil sequences, western Sichuan Province, southwest China. Paleogeogr. Paleoclimatol. Paleoecol. 414, 192—199.

Rodés, Á., Pallàs, R., Braucher, R., Moreno, X., Masana, E., Bourlès, D.L., 2011. Effect of density uncertainties in cosmogenic [10]Be depth-profiles: dating a cemented Pleistocene alluvial fan (Carboneras Fault, SE Iberia). Quat. Geochronol. 6, 186—194.

Rodés, Á., Pallàs, R., Ortuño, M., García-Melendez, E., Masana, E., 2014. Combining surface exposure dating and burial dating from paired cosmogenic depth profiles. Example of El Límite alluvial fan in Huércal-Overa basin (SE Iberia). Quat. Geochronol. 19, 127—134.

Roger, F., Jolivet, M., Malavieille, J., 2008. Tectonic evolution of the Triassic fold belts of Tibet. C. R. Geosci. 340, 180—189.

Roger, F., Jolivet, M., Malavieille, J., 2010. The tectonic evolution of the Songpan-Garzê (North Tibet) and adjacent areas from Proterozoic to Present: a synthesis. J. Asian Earth Sci. 39, 254—269.

Rohling, E.J., Hibbert, F.D., Williams, F.H., Grant, K.M., Marino, G., Foster, G.L., Hennekam, R., de Lange, G.J., Roberts, A.P., Yu, J., Webster, J.M., Yokoyama, Y., 2017. Differences between the last two glacial maxima and implications for ice-sheet, $\delta^{18}O$, and sea-level reconstructions. Quat. Sci. Rev. 176, 1—28.

Royden, L.H., Burchfiel, B.C., King, R.W., Wang, E., Chen, Z., Shen, F., Liu, Y., 1997. Surface deformation and lower crustal flow in eastern Tibet. Science 276, 788—790.

Ruszkiczay-Rüdiger, Z., Braucher, R., Novothny, Á., Csillag, G., Fodor, L., Molnár, P., Madarász, B., 2016. Tectonic and climatic control on terrace formation: coupling in situ produced [10]Be depth profiles and luminescence approach, Danube River, Hungary, Central Europe. Quat. Sci. Rev. 131, 127—147.

Saint-Carlier, D., Charreau, J., Lavé, J., Blard, P.-H., Dominguez, S., Avouac, J.-P., Wang, S., 2016. Major temporal variations in shortening rate absorbed along a large active fold of the southeastern Tianshan piedmont (China). Earth Planet. Sci. Lett. 434, 333—348.

Schäfer, J.M., Tschudi, S., Zhao, Z., Wu, X., Ivy-Ochs, S., Wieler, R., Baur, H., Kubik, P.W., Schlüchter, C., 2002. The limited influence of glaciations in Tibet on global climate over the past 170 000 yr. Earth Planet. Sci. Lett. 194, 287–297.

Schaller, M., Ehlers, T.A., Lang, K.A.H., Schmid, M., Fuentes-Espoz, J.P., 2018. Addressing the contribution of climate and vegetation cover on hillslope denudation, Chilean Coastal Cordillera (26°–38°S). Earth Planet. Sci. Lett. 489, 111–122.

Schaller, M.F., von Blanckenburg, F., Veldkamp, A., Tebbens, L.A., Hovius, N., Kubik, P.W., 2002. A 30000 yr record of erosion rates from cosmogenic [10]Be in Middle European river terraces. Earth Planet. Sci. Lett. 204, 307–320.

Schumer, R., Jerolmack, D.J., 2009. Real and apparent changes in sediment deposition rates through time. J. Geophys. Res. 114, F00A06.

Siame, L., Bellier, O., Braucher, R., Sébrier, M., Cushing, M., Bourlès, D., Hamelin, B., Baroux, E., de Voogd, B., Raisbeck, G., Yiou, F., 2004. Local erosion rates versus active tectonics: cosmic ray exposure modelling in Provence (south-east France). Earth Planet. Sci. Lett. 220, 345–364.

Sordi, V.D.M., Salgado, A.A.R., Siame, L., Bourlès, D., Paisani, J.C., Léanni, L., Braucher, R., Couto, V.d.E., Team, A., 2018. Implications of drainage rearrangement for passive margin escarpment evolution in southern Brazil. Geomorphology 306, 155–169.

Stone, J.O., 2000. Air pressure and cosmogenic isotope production. J. Geophys. Res. Solid Earth 105, 23753–23759.

Strasky, S., Graf, A.A., Zhao, Z., Kubik, P.W., Baur, H., Schlüchter, C., Wieler, R., 2009. Late Glacial ice advances in southeast Tibet. J. Asian Earth Sci. 34, 458–465.

Tapponnier, P., Xu, Z., Roger, F., Meyer, B., Arnaud, N., Wittlinger, G., Yang, J., 2001. Oblique stepwise rise and growth of the Tibet plateau. Science 294, 1671–1677.

Taylor, M., Yin, A., 2009. Active structures of the Himalayan-Tibetan orogen and their relationships to earthquake distribution, contemporary strain field, and Cenozoic volcanism. Geosphere 5, 199–214.

Tian, Y., Li, R., Tang, Y., Xu, X., Wang, Y., Zhang, P., 2018. Thermochronological constraints on the late Cenozoic morphotectonic evolution of the Min Shan, the eastern margin of the Tibetan plateau. Tectonics 37, 1733–1749.

Tschudi, S., Schäfer, J.M., Zhao, Z., Wu, X., Ivy-Ochs, S., Kubik, P.W., Schlüchter, C., 2003. Glacial advances in Tibet during the younger Dryas? Evidence from cosmogenic [10]Be, [26]Al, and [21]Ne. J. Asian Earth Sci. 22, 301–306.

Vermeesch, P., 2007. CosmoCalc: an Excel add-in for cosmogenic nuclide calculations. Geochem. Geophys. Geosyst. 8, Q08003.

Wang, E., Burchfiel, B.C., 2000. Late Cenozoic to Holocene deformation in southwestern Sichuan and adjacent Yunnan, China, and its role in formation of the southeastern part of the Tibetan Plateau. Geol. Soc. Am. Bull. 112, 413–423.

Wang, E., Kirby, E., Furlong, K.P., van Soest, M., Xu, G., Shi, X., Kamp, P.J.J., Hodges, K.V., 2012. Two-phase growth of high topography in eastern Tibet during the Cenozoic. Nat. Geosci. 5, 640–645.

Wang, J., Raisbeck, G.M., Xu, X., Yiou, F., Bai, S., 2006. In situ cosmogenic [10]Be dating of the Quaternary glaciations in the southern Shaluli Mountain on the Southeastern Tibetan Plateau. Sci. China Ser. D Earth Sci. 49, 1291–1298.

Wang, Y.J., Cheng, H., Edwards, R.L., An, Z.S., Wu, J.Y., Shen, C.C., Dorale, J.A., 2001. A high-resolution absolute-dated late Pleistocene Monsoon record from Hulu Cave, China. Science 294, 2345–2348.

Whipple, K.X., 2004. Bedrock rivers and the geomorphology of active orogens. Annu. Rev. Earth Planet Sci. 32, 151–185.

Whipple, K.X., 2009. The influence of climate on the tectonic evolution of mountain belts. Nat. Geosci. 2, 97.

Whipple, K.X., Tucker, G.E., 2002. Implications of sediment-flux-dependent river incision models for landscape evolution. J. Geophys. Res. Solid Earth 107. ETG 3-1-ETG 3-20.

Wittmann, H., von Blanckenburg, F., Maurice, L., Guyot, J.L., Kubik, P.W., 2011. Recycling of Amazon floodplain sediment quantified by cosmogenic [26]Al and [10]Be. Geology 39, 467–470.

Wu, T., Xiao, L., Wilde, S.A., Ma, C.-Q., Zhou, J.-X., 2017. A mixed source for the Late Triassic Garzê-Daocheng granitic belt and its implications for the tectonic evolution of the Yidun arc belt, eastern Tibetan Plateau. Lithos 288–289, 214–230.

Xu, L., Ou, X., Lai, Z., Zhou, S., Wang, J., Fu, Y., 2010. Timing and style of late pleistocene glaciation in the Queer Shan, northern Hengduan mountains in the eastern Tibetan plateau. J. Quat. Sci. 25, 957–966.

Xu, L., Zhou, S., 2009. Quaternary glaciations recorded by glacial and fluvial landforms in the Shaluli Mountains, Southeastern Tibetan Plateau. Geomorphology 103, 268–275.

Xu, X., Wang, J., Zhu, J., Jiang, H., Yang, Y., 2004. Study on glacial erosion surface of the southeast of Qinghai-Xizang Plateau using cosmogenic isotopes dating. Sci. Geogr. Sin. 24, 101–104 (in Chinese with English abstract).

Yan, B., Lin, A., 2017. Holocene activity and paleoseismicity of the Selaha fault, southeastern segment of the strike-slip Xianshuihe Fault zone, Tibetan plateau. Tectonophysics 694, 302–318.

Yin, A., Harrison, T.M., 2000. Geologic evolution of the Himalayan-Tibetan orogen. Annu. Rev. Earth Planet Sci. 28, 211–280.

Yuan, D., Cheng, H., Edwards, R.L., Dykoski, C.A., Kelly, M.J., Zhang, M., Qing, J., Lin, Y., Wang, Y., Wu, J., Dorale, J.A., An, Z., Cai, Y., 2004. Timing, duration, and transitions of the last interglacial Asian monsoon. Science 304, 575–578.

Zhang, B., Ou, X., Lai, Z., 2012. OSL ages revealing the glacier retreat in the Dangzi valley in the eastern Tibetan Plateau during the Last Glacial Maximum. Quat. Geochronol. 10, 244–249.

Zhang, J., Liu-Zeng, J., Scherler, D., Yin, A., Wang, W., Tang, M., Li, Z., 2018. Spatiotemporal variation of late Quaternary river incision rates in southeast Tibet, constrained by dating fluvial terraces. Lithosphere 10, 662–675.

Zhang, Z., Wang, J., Xu, X., BAI, S., Chang, Z.Y., 2015. Cosmogenic [10]Be and [26]Al chronology of the last glaciation of the palaeo-Daocheng ice cap, southeastern Qinghai-Tibetan plateau. Acta Geol. Sin. (Engl. Ed.) 89, 575–584.

Zhao, Z.J., Liu, Y., Chen, Y., Zhang, M.H., Shu, Q., Li, C.L., 2013. Quaternary fluvial incision rates of the Western Sichuan Plateau inferred from ESR chronology. J. Lanzhou Univ. 49, 160–172 (in Chinese with English abstract).

Zhou, S., Xu, L., Cui, J., Zhang, X., Zhao, J., 2005. Geomorphologic evolution and environmental changes in the Shaluli Mountain region during the Quaternary. Chin. Sci. Bull. 50, 52–57.